Iron Intermetallic Phases in the Al Corner of the Al-Si-Fe System

W. KHALIFA, F.H. SAMUEL, and J.E. GRUZLESKI

The iron intermetallics observed in six dilute Al-Si-Fe alloys were studied using thermal analysis, optical microscopy, and image, scanning electron microscopy/energy dispersive X-ray, and electron probe microanalysis/wavelength dispersive spectroscopy (EPMA/WDS) analyses. The alloys were solidified in two different molds, a preheated graphite mold (600 °C) and a cylindrical metallic mold (at room temperature), to obtain slow (~0.2 °C/s) and rapid (~15 °C/s) cooling rates. The results show that the volume fraction of iron intermetallics obtained increases with the increase in the amount of Fe and Si added, as well as with the decrease in cooling rate. The low cooling rate produces larger-sized intermetallics, whereas the high cooling rate results in a higher density of intermetallics. Iron addition alone is more effective than either Si or Fe + Si additions in producing intermetallics. The alloy composition and cooling rate control the stability of the intermetallic phases: binary Al-Fe phases predominate at low cooling rates and a high Fe:Si ratio; the β-Al_5FeSi phase is dominant at a high Si content and low cooling rate; the α-iron intermetallics (*e.g.*, α-Al_8Fe_2Si) exist between these two; while Si-rich ternary phases such as the δ-iron Al_4FeSi_2 intermetallic are stabilized at high cooling rates and Si contents of 0.9 wt pct and higher. Calculations of the solidification paths representing segregations of Fe and Si to the liquid using the Scheil equation did not conform to the actual solidification paths, due to the fact that solid diffusion is not taken into account in the equation. The theoretical models of Brody and Flemings[44] and Clyne and Kurz[45] also fail to explain the observed departure from the Scheil behavior, because these models give less weight to the effect of solid back-diffusion. An adjusted 500 °C metastable isothermal section of the Al-Si-Fe phase diagram has been proposed (in place of the equilibrium one), which correctly predicts the intermetallic phases that occur in this part of the system at low cooling rates (~0.2 °C/s).

I. INTRODUCTION

COMMERCIAL unalloyed aluminums and aluminum-base alloys contain a considerable amount of iron and silicon as impurities or alloying additions. Commercial aluminum alloys, which have up to 1 pct of iron and silicon, can be considered ternary alloys. Because the solid solubility of iron in aluminum is less than 0.05 pct at equilibrium, nearly all iron in aluminum alloys forms second-phase particles. Both iron and silicon have partition coefficients less than unity, and accordingly segregate to the liquid between the Al dendrite arms during the course of solidification. Therefore, when considering the nonequilibrium lever-rule assumption,[1] primary particles of binary Al-Fe and ternary Al-Fe-Si phases, and even silicon, can form during casting of an aluminum-rich alloy. The chemical composition and local cooling rate are the controlling factors that determine which phases will form[2,3] and their particle size.[4,5]

An extensive review of the Al-Fe-Si system has been published by Rilvin and Raynor.[6] Several studies by other workers,[7,8,9] have focused upon the Al-rich part of the system, where the θ-Al_3Fe, α-AlFeSi, and β-AlFeSi phases have been reported as equilibrium phases.[9,10] In addition, some nonequilibrium phases have been identified, for example, metastable phases such as Al_6Fe,[3,11,12] Al_m Fe,[13,14] and Al_xFe[3,15] instead of the θ-Al_3Fe (or θ-$Al_{13}Fe_4$)[16,17] equilibrium phase. Structures of various phases, *e.g.*, Al_6Fe,[13,18] Al_3Fe,[11,19] and α-AlFeSi[20,21,22] have been investigated. The complex structure of Al_mFe has also been suggested.[23,24]

Without doubt, the binary Al-Fe and ternary Al-Fe-Si phases constitute an important part of the microstructure in aluminum alloys. Particles formed during casting may influence the material properties during subsequent fabrication steps or in service. For example, the β-AlFeSi platelike phase has a detrimental influence on the alloy properties. The β-phase platelets act as potential sites for crack initiation, which, consequently, results in decohesion failure.[25] Other phases such as Al_3Fe and α-AlFeSi are cathodic to the aluminum matrix, and when present on the surface, promote pitting attack of the surface in conductive liquids.[26] Thus, control of these phases is of considerable technological importance.

In view of the importance of iron intermetallic phases in aluminum alloys, this study was carried out to characterize their precipitation as affected by (1) the chemical composition, through the use of six dilute alloys covering the Al corner of the Al-Si-Fe system, and (2) the cooling rate, where two ranges of cooling rates were employed: a slow cooling rate range (0.16 °C/s to 0.21 °C/s) resembling the sand casting condition, and a high cooling rate range (10 °C/s to 15 °C/s), similar to the cooling rates observed in pressure die casting processes. Experiments in this study were designed to determine the iron intermetallic phases that might form in the group of alloys, as a first part of a project, which aims to study the nucleation of these phases on the surface of certain inclusions.

W. KHALIFA, Ph. D. Student, and F.H. SAMUEL, Professor, are with the Département des Sciences Appliquées, University of Quebec at Chicoutimi (UQAC), Chicoutimi, PQ, Canada G7H 2B1. Contact e-mail: fhsamuel@uqac.ca J.E. GRUZLESKI, Professor, Department of Mining, Metals and Materials Engineering, and Dean, Faculty of Engineering, is with McGill University, Montreal, PQ, Canada H3A 2B2.

Manuscript submitted March 15, 2002.

Table I. Compositions of the Al-Si-Fe Alloys Used in the Present Work

	Element, Wt Pct								
Alloy	Si	Fe	Cu	Mn	Mg	Bi	La	V	Ga
1	0.35	0.23	0.0033	<0.0005	0.0015	<0.0025	0.0094	0.0041	0.0087
2	0.49	0.23	0.0057	<0.0005	0.0017	<0.0025	0.0094	0.0042	0.0086
3	0.62	0.55	0.0040	<0.0005	0.0009	<0.0025	0.0091	0.0038	0.0088
4	0.90	0.56	0.0035	0.0006	0.0014	<0.0025	0.0091	0.0040	0.0089
5	0.62	1.03	0.0043	0.0032	0.0013	<0.0025	0.0088	0.0042	0.0091
6	6.32	0.52	0.0030	0.0007	0.0011	<0.0025	0.0090	0.0045	0.0082

II. EXPERIMENTAL

The chemical compositions of the six alloys investigated are shown in Table I (each composition representing the average of three spectroanalyses). This group of experimental alloys is representative of the Al-rich corner of the Al-Si-Fe system. The alloys were prepared from high-purity components to avoid any contamination that could arise from the use of commercial purity materials.

Alloys 1 and 2, with the same iron level (0.23 wt pct) but different silicon levels, were proposed in order to study the effect of Si content when the Fe level is low. Alloys 3 and 4 are the analogs of alloys 1 and 2, with nearly double concentrations of iron and silicon. These compositions enable us to study the effect of a higher Fe content as well as that of an increase in Si content. Only alloy 5 has higher iron than silicon (1.03 and 0.62 pct, respectively), and was proposed in order to evaluate the effect of a very high Fe level such as those often encountered in commercial alloys. Alloy 6, with its high Si level (6.32 pct) and and Fe level of 0.52 pct, was selected as being representative of commercial Al-Si alloys. These compositions were selected very carefully, with a view to investigating the occurrence of the different iron intermetallic phases that can form in dilute aluminum alloys. The total Fe + Si alloying (or impurity element) content increases gradually from alloy 1 through alloy 6. This group of experimental alloys is representative of the Al-rich corner of the Al-Si-Fe system and was selected precisely for this reason.

Thermal analysis tests were performed for the six alloys over a wide range of cooling rates (*i.e.*, solidification times) as follows. Alloy melts were poured into (1) a graphite mold preheated to ~600 °C, which provided the lowest cooling rates (0.16 °C/s to 0.21 °C/s, depending on the alloy), and (2) a cylindrical metallic mold with decreasing wall thickness, kept at room temperature that provided high cooling rates (10 °C/s to 15 °C/s). When the ingots' temperature reached 500 °C, the ingots were brought to the ambient temperature by forced cooling in running water. Hereafter, the terms "metallic mold" and "graphite mold" will be taken to represent the high cooling and low cooling conditions, respectively. Figure 1 shows the schematic diagram for the two molds.

The thermal analysis was carried out using chromel-alumel type-K thermocouples and Strawberry Tree software (Strawberry Tree Inc., Sunnyvale, CA) to obtain the cooling curves corresponding to each alloy and mold system. In the case of the graphite mold, a two-thermocouple system similar to that used by Backerud *et al.*[27] was employed for accuracy (Figure 1(a)). The starting and termination points of a reaction were also determined according to the definitions given by Backerud *et al.*

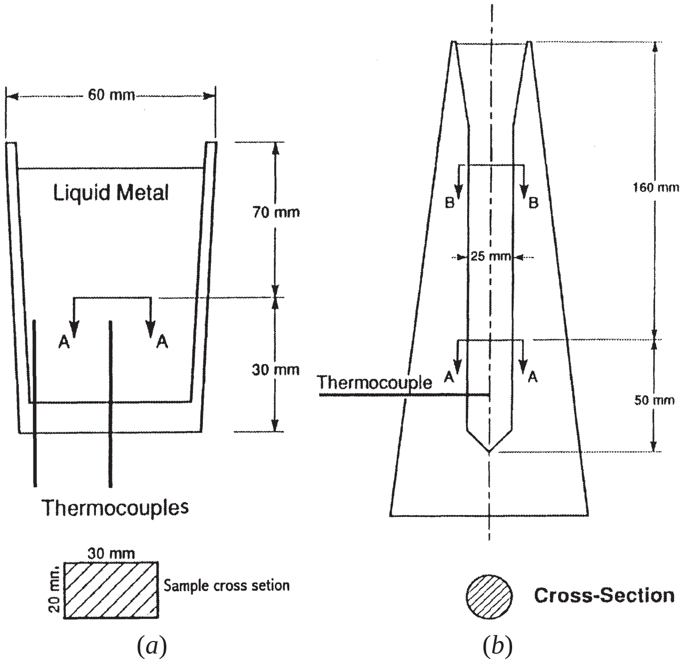

(*a*) (*b*)

Fig. 1—Schematic diagram of the (*a*) graphite and (*b*) metallic molds used to prepare alloy castings.

For the purpose of studying the microstructure and various phases that were obtained corresponding to the different cooling conditions, samples were sectioned near the thermocouple tip (Figure 1), mounted and polished for metallographic examination.

Both optical and scanning electron microscopy were used to examine the microstructure. Quantitative analysis of the volume fractions of the various phases and their particle characteristics were carried out using a LECO* 2001 image analyzer. Mapping of some specific areas of the polished sample surfaces was also done to determine the distribution of alloying elements between phases. Electron probe microanalysis (EPMA) and wavelength dispersive spectroscopy (WDS) analysis of the intermetallic phases was carried out using a JEOL** WD/ED combined microanalyzer (model JXA-8900R), operating at 20 kV and 30 nA (electron beam size of ~1 μm).

---

*LECO is a trademark of LECO Corporation, St. Joseph, MI.

**JEOL is a trademark of Japan Electron Optics Ltd., Tokyo.

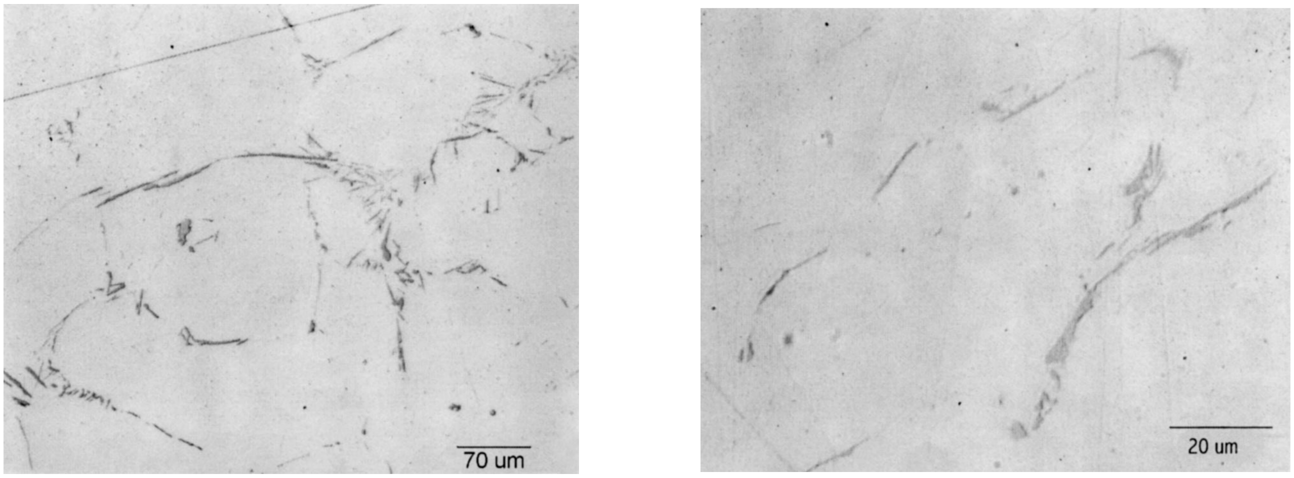

(*a*) (*b*)

Fig. 2—Microstructures of alloy 1 obtained from (*a*) graphite mold (cooling rate 0.16 °C/s) and (*b*) metallic mold (cooling rate 10.7 °C/s) castings.

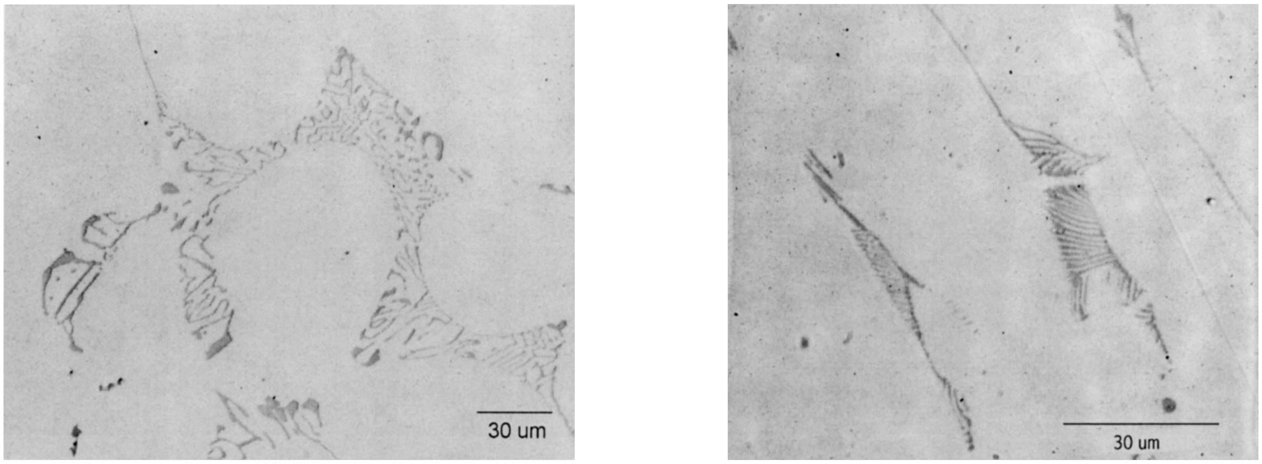

(*a*) (*b*)

Fig. 3—Microstructures of alloy 2 obtained from (*a*) graphite mold (cooling rate 0.16 °C/s) and (*b*) metallic mold (cooling rate 13.8 °C/s) castings.

III. RESULTS AND DISCUSSION

As mentioned in Section II, metallographic samples were sectioned from the graphite mold and metallic mold castings close to the thermocouple tip and polished for microstructural examination. Therefore, the corresponding microstructure may be considered as representative of the solidification conditions recorded by the thermocouples. It should be mentioned here that, although results for all alloys have been described in detail, for the sake of brevity, not all microstructures and cooling curves have been depicted.

IV. OPTICAL MICROSCOPY AND IMAGE ANALYSIS

The optical micrographs of Figures 2 through 5 show how the microstructure varies with alloy composition. The intermetallic phases that form in this part of the Al-Si-Fe system are mainly iron-bearing phases (grouped together hereafter as iron intermetallics). The microstructures of alloy 1 shown in Figure 2 reveal that, in general, the intermetallic phases form in the interdendritic regions. At a slow cooling rate (0.16 °C/s), the microstructure contains needlelike phases and fine eutectic regions (Figure 2(a)). At a high cooling rate (10.7 °C/s), the microstructure is extremely fine (Figure 2(b)).

Microstructures of alloys 2 and 3 (not shown) contained almost only iron intermetallic phases with dendritic (or so-called Chinese script) morphologies, in addition to the aluminum matrix, when cooled slowly in the graphite mold (Figure 3(a)), which changed to finer lamellar and platelike phases when the alloys were cooled in the metallic mold (Figure 3(b)). Two types of intermetallic phases were observed in the microstructure of the graphite mold-cast alloy 4 sample: a dendritic or Chinese script-like phase (α-AlFeSi) and a platelike phase (β-AlFeSi). In the fast-cooled sample, however, only the platelike δ-AlFeSi phase was observed, as is clear from Figure 4.

Alloy 5 exhibits a diversity of phases at slow cooling rate, which could not be differentiated by the image analyzer, because of their similar gray levels, as seen in Figure 5(a). The fast-cooled sample of alloy 5 (Figure 5(b)), exhibited a fine fibrous phase and a dendritic phase. Coarse eutectic silicon and large platelets of β-AlFeSi were observed in alloy 6 after slow cooling, whereas at the high cooling rate (12.8 °C/s), the structure exhibited fine, modified eutectic areas delineating the aluminum dendrites, and a light gray phase (δ-AlFeSi) in the interdendritic regions.

The similar gray levels of the intermetallic phases impeded their quantitative measurement, because various phases could not be distinguished from each other by the image analysis system. It should be mentioned here that the LECO image analyzer recognizes various phases depending on their gray level, which can range over a scale of 0 to 250 (0 representing the black and 250 representing the white end of the range). The threshold level for each phase is set by the observer and, once set, the machine measures the volume fraction or other characteristics of the phase based upon these levels. In addition, as there appeared to be no remarkable differences in the morphology of these phases, particularly in alloys 1 and 5, the quantitative analysis was carried out for all the iron intermetallics grouped together.

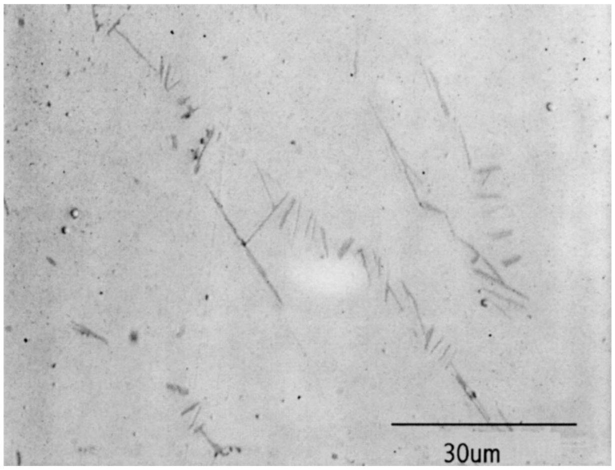

Fig. 4—Microstructure of alloy 4 obtained from metallic mold casting (cooling rate 12.8 °C/s).

Volume fractions of all iron intermetallic phases were measured for each alloy condition, and the results are plotted in the histogram shown in Figure 6. As can be seen, the volume fraction of iron intermetallics increases as the Si + Fe content increases, from alloy 1 to alloy 6, for both conditions of cooling. Obviously, solidification in the graphite mold at slow cooling rates/longer solidification times resulted in a larger volume fraction of intermetallics compared to that obtained with the metallic mold-cast samples. The largest volume fraction of intermetallics was recorded for alloy 5, containing 1.03 pct Fe and 0.62 pct Si. Analysis of Figure 6 shows that the Fe content is more important than either the Si or the Si + Fe contents in determining the volume fraction of iron intermetallics formed. The effect of silicon is less evident, as demonstrated by the negligible difference in the volume fractions of iron intermetallics obtained in alloys 1 and 2 and in alloys 3 and 4.

Figure 7 shows the plots of (a) average particle lengths and (b) densities obtained from quantitative analysis of the Fe intermetallics observed in the six alloys. Owing to the fact that slow cooling (*i.e.*, a longer solidification time) enhances the growth of phases during solidification, the lengths of the Fe intermetallics are longer in the graphite mold-cast samples compared to those obtained from the metallic mold (Figure 7 (a)). The latter samples, however, display higher densities, which is in accordance with the fact that a greater number of smaller-sized Fe intermetallics are expected to precipitate at the higher cooling rate, to compensate for the total volume fraction of intermetallics estimated to result in a specified alloy (depending upon its Fe and Si contents). In general, under both cooling conditions, the density is observed to increase with the increase in the Fe + Si content, as one proceeds from alloy 1 to alloy 6.

V. SCANNING ELECTRON MICROSCOPY, WDS ANALYSIS, AND THERMAL ANALYSIS

As mentioned previously, although results for all alloys have been described in detail, for the sake of brevity, not all microstructures and cooling curves have been shown.

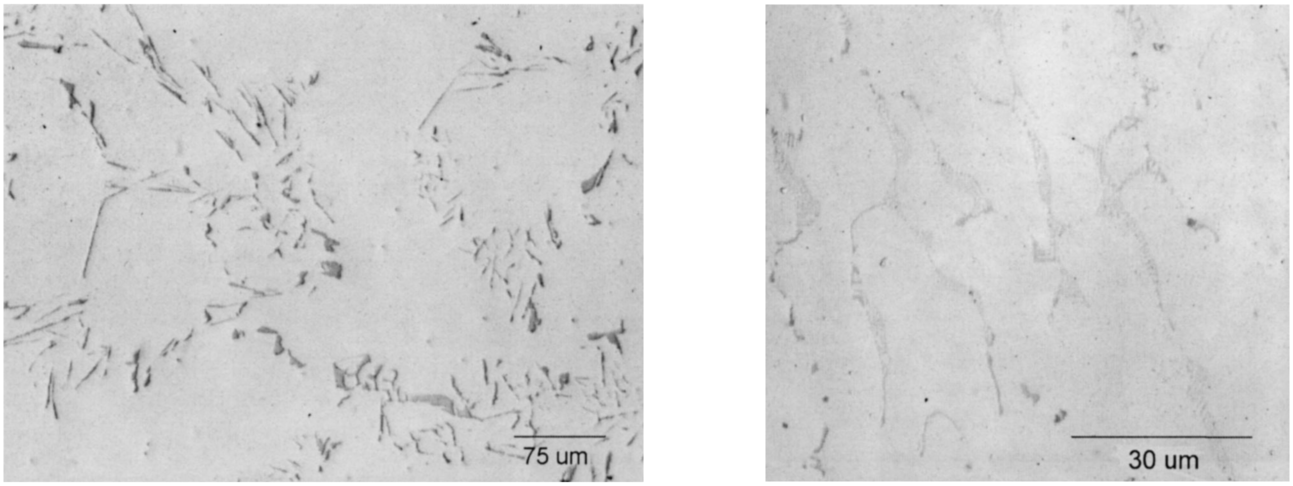

(*a*) (*b*)

Fig. 5—Microstructures of alloy 5 obtained from (*a*) graphite mold (cooling rate 0.19 °C/s) and (*b*) metallic mold (cooling rate 14.3 °C/s) castings.

VI. OBSERVED PHASES

A. *Alloy 1 (0.23 Pct Fe + 0.35 Pct Si)*

The structure of alloy 1 contains only binary iron intermetallic phases when solidified slowly, but also some ternary phases after rapid cooling. The results of the WDS analysis carried out on these phases are summarized in Table II, and correspond to the backscattered images shown in Figure 8 for the alloy 1 sample cooled at ~0.16 °C/s. Three binary iron intermetallics were identified, namely, $\mathrm{Al}_m\mathrm{Fe}$, $\mathrm{Al}_6\mathrm{Fe}$, and $\mathrm{Al}_x\mathrm{Fe}$. The composition of $\mathrm{Al}_m\mathrm{Fe}$ was 64.84 wt pct Al, 33.8 wt pct Fe, and 1.6 wt pct Si, corresponding to $m = 4$. Values of $m = 4.2$[28] and $m = 4.4$[17] have been ascribed to the phase previously by other workers. The $\mathrm{Al}_6\mathrm{Fe}$ phase, which has the highest aluminum content among all the iron intermetallic phases, was nearly stoichiometeric, as previously reported by Porter and Westengen[14] and Westengen.[17] Its composition was 73.4 wt pct Al, 26.5 wt pct Fe, and 1.5 wt pct Si. It can be seen from Table II that the chemical composition of $\mathrm{Al}_x\mathrm{Fe}$ is 70.72 wt pct Al, 26.1 wt pct Fe, and 1.7 wt pct Si, which corresponds to $x = 5.6$. The structure of this phase is not known. It has been reported to have a defective crystal structure and a chemical composition corresponding to $x = 5.8$.[17] The formation of these three metastable phases at a very low cooling rate (0.16 °C/s) is in direct contrast to the findings of Miki *et al.*[2] Young,[3] and Kosuge and Mizukami.[29] According to these studies, the $\mathrm{Al}_3\mathrm{Fe}$ phase is stable when obtained at cooling rates below 1 °C/s, the $\mathrm{Al}_x\mathrm{Fe}$ phase between 0.5 °C/s and 6 °C/s[3], and the $\mathrm{Al}_6\mathrm{Fe}$ phase at cooling rates in the ranges 1 °C/s^2 to 10 °C/s^2, 3 °C/s^3 to 18 °C/s^3, or 2 °C/s to 20 °C/s.[29] The $\mathrm{Al}_m\mathrm{Fe}$ phase is reported to be stable when obtained at cooling rates above 10 °C/s,[2] 18 °C/s,[3] or 20 °C/s.[29] Apparently, the difference in results between these studies and ours can be attributed to the commercial grade DC casting alloys used in the former, containing much higher Fe/Si ratios, whereas in our study, the Si content is considerably high, in fact, higher than that of iron in most cases. For example, Kosuge and Mizukam used an alloy containing 0.58 wt pct Fe and 0.01 wt pct Si, while Miki *et al.* used Fe/Si ratios close to 10.

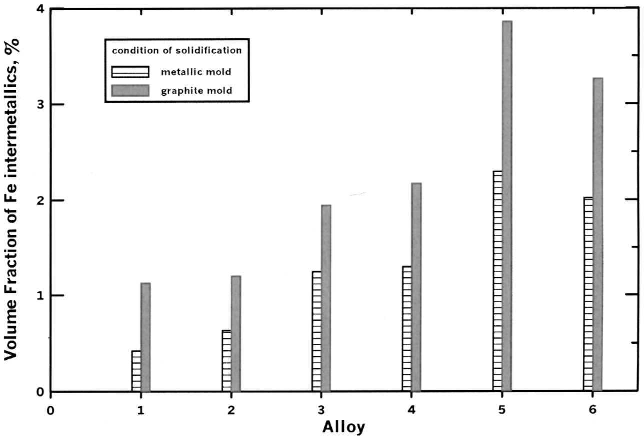

Fig. 6—Volume fraction of iron intermetallics observed in the alloys studied, as a function of solidification condition.

From a comparison of these results, it can be deduced that Si stabilizes metastable Al-Fe phases such as $\mathrm{Al}_m\mathrm{Fe}$, $\mathrm{Al}_6\mathrm{Fe}$, and $\mathrm{Al}_x\mathrm{Fe}$ at slow cooling rates (0.16 °C/s). In other words, Si shifts the cooling rates that are required for the stability of the binary $\mathrm{Al}_m\mathrm{Fe}$, $\mathrm{Al}_6\mathrm{Fe}$, and $\mathrm{Al}_x\mathrm{Fe}$ phases to very low values. In addition, these phases have been reported to contain small amounts of silicon in their composition,[22] a fact that is confirmed in the present work (to be discussed later). From the absence of $\mathrm{Al}_3\mathrm{Fe}$ in the microstructure of alloy 1, and according to the results of Miki *et al.*[2] and Kosuge and Mizukam,[29] it can be suggested that silicon stabilizes the

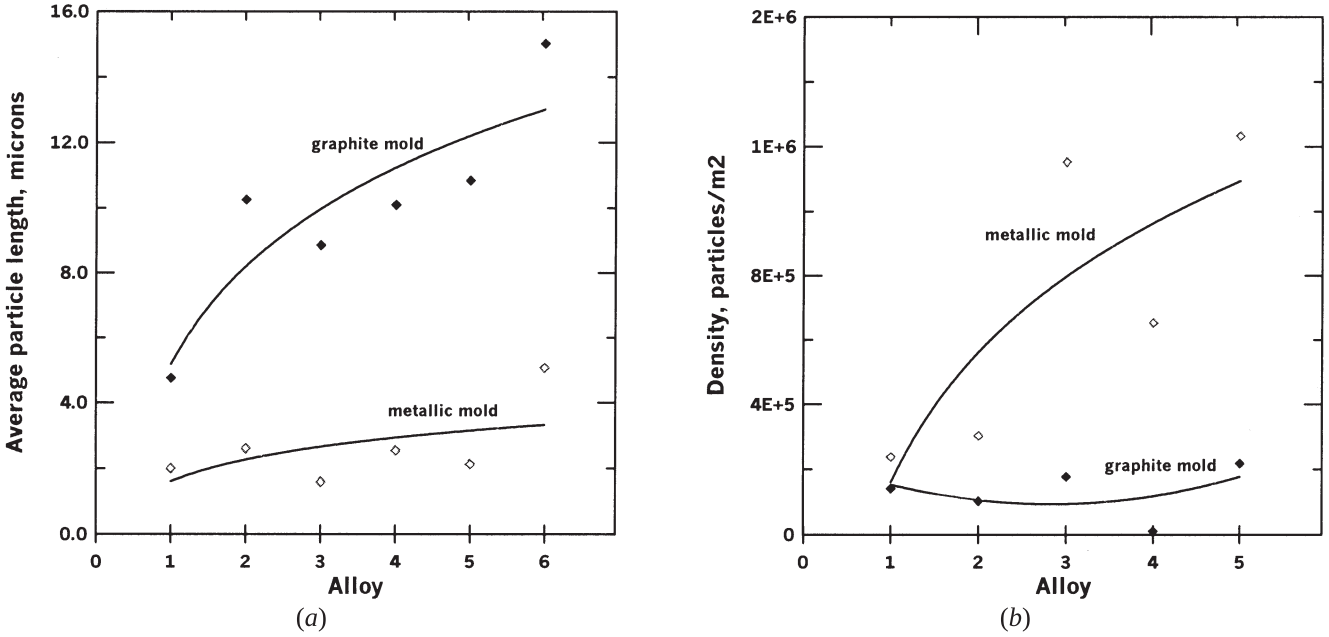

(*a*) (*b*)

Fig. 7—Quantitative analysis of the iron intermetallics observed in different alloy samples obtained from the graphite and metallic mold castings: (*a*) average particle length and (*b*) density.

Table II. WDS Analysis of Iron Intermetallic Phases Observed in the Present Study (as Shown in Figure 18)

	Composition, Wt Pct					Stoichiometry, Fe/Si Atomic Ratio	Condition	
Phase	Al	Si	Fe	Cu	Mn+Cr		Alloy	Cooling Rate, °C/s
Al_mFe	63.23	1.53	33.31	0.040	0.026	$Al_{3.93}FeSi_{0.091}$	1	0.16
	66.45	1.63	34.20	0.0057	0.016	$Al_{4.02}FeSi_{0.095}$		
	65.94	1.72	32.15	0.000	0.045	$Al_{4.25}FeSi_{0.11}$	5	0.19
Al_6Fe	73.44	1.49	25.94	0.044	0.02	$Al_{6.05}FeSi_{0.114}$	1	0.16
	73.30	1.59	27.04	0.005	0.024	$Al_{6.02}FeSi_{0.117}$		
	73.16	1.76	25.92	0.017	0.033	$Al_{6.10}FeSi_{0.14}$	5	0.19
Al_xFe	70.72	1.69	26.12	0.032	0.019	$Al_{5.60}FeSi_{0.128}$	1	0.16
Al_3Fe	61.85	1.45	37.15	0.038	0.044	$Al_{3.43}FeSi_{0.08}$	5	0.19
α-AlFeSi	63.59	7.61	30.45	0.050	0.025	$Al_{8.7}Fe_{2.0}Si$	2	0.16
	69.12	7.68	26.62	0.057	0.037	$Al_{11.18}Fe_2Si_{1.15}$		
	69.85	7.65	25.22	0.028	0.041	$Al_{11.45}Fe_2Si_{1.2}$		
	68.78	8.07	25.71	—	—	$Al_{11.08}Fe_2Si_{1.25}$	3	0.21
	74.48	7.38	26.42	—	—	$Al_{11.67}Fe_2Si_{1.11}$		
						Fe : Si = 2 : 1.36	3	14.7
						Fe : Si = 2 : 1.11		
	59.46	8.06	30.37	0.81	0.085	$Al_{8.12}Fe_2Si_{1.06}$	4	0.18
	62.05	7.87	30.07	0.45	0.125	$Al_{8.55}Fe_2Si_{1.04}$		
	62.36	8.61	30.21	0.43	—	$Al_{8.59}Fe_2Si_{1.14}$		
	62.73	9.34	30.28	0.46	—	$Al_{8.60}Fe_2Si_{1.23}$		
	62.91	8.08	30.17	0.32	—	$Al_{8.65}Fe_2Si_{1.06}$		
	66.89	8.38	23.91	0.42	—	$Al_{11.65}Fe_2Si_{1.4}$		
	60.80	9.11	29.71	0.076	0.035	$Al_{8.47}Fe_2Si_{1.2}$	5	0.19
	62.76	9.24	29.48	0.050	0.049	$Al_{8.81}Fe_2Si_{1.25}$		
	67.59	6.71	30.75	0.042	0.053	$Al_{9.1}Fe_2Si_{0.87}$		
	67.46	7.29	26.79	0.039	0.029	$Al_{10.42}Fe_2Si_{1.08}$		
	73.01	6.87	23.88	0.065	0.030	$Al_{12.66}Fe_2Si_{1.14}$		
						Fe:Si=2 : 1.16	5	14.3
β-AlFeSi	58.97	13.06	26.42	0.042	0.036	$Al_{4.60}FeSi_{0.98}$	4	0.18
	59.04	14.69	26.59	0.059	0.056	$Al_{4.59}FeSi_{1.10}$		
	61.39	14.37	26.41	0.01	—	$Al_{4.84}FeSi_{1.09}$		
	63.52	14.43	26.25	0.02	—	$Al_{4.98}FeSi_{1.09}$		
	55.31	14.79	26.99	0.022	0.061	$Al_{4.24}FeSi_{1.09}$	6	0.18
	55.32	15.25	26.86	0.00	0.097	$Al_{4.20}FeSi_{1.13}$		
	55.57	14.90	26.90	0.00	0.071	$Al_{4.27}FeSi_{1.04}$		
	57.46	14.68	26.47	0.119	0.221	$Al_{4.50}FeSi_{1.10}$		
	56.47	14.61	26.70	0.031	0.213	$Al_{4.38}FeSi_{1.09}$		
	57.27	14.75	26.64	0.099	0.206	$Al_{4.67}FeSi_{1.14}$		
	55.31	14.79	26.99	0.022	0.061	$Al_{4.24}FeSi_{1.09}$		
	55.32	15.25	26.86	0.00	0.097	$Al_{4.20}FeSi_{1.13}$		
						Fe : Si = 1 : 0.91	1	10.7
						Fe : Si = 1 : 1.13	2	13.8
δ-AlFeSi or δ-β composite particles						Fe : Si = 1 : 1.52	1	10.7
						Fe : Si = 1 : 1.31	2	13.8
						Fe : Si = 1 : 1.38		
						Fe : Si = 1 : 1.37	3	14.7
						Fe : Si = 1 : 2.08	4	12.8
						Fe : Si = 1 : 1.53		
						Fe : Si = 1 : 1.50		
						Fe : Si = 1 : 2.50	6	12.8
						Fe : Si = 1 : 3		
						Fe : Si = 1 : 2.23		
q_1-AlFeSi	86.26	4.77	12.02	—	—	$Al_{14.9}FeSi_{0.79}$	2	13.8
	83.69	4.34	13.03	—	—	$Al_{13.2}FeSi_{0.66}$	5	14.3

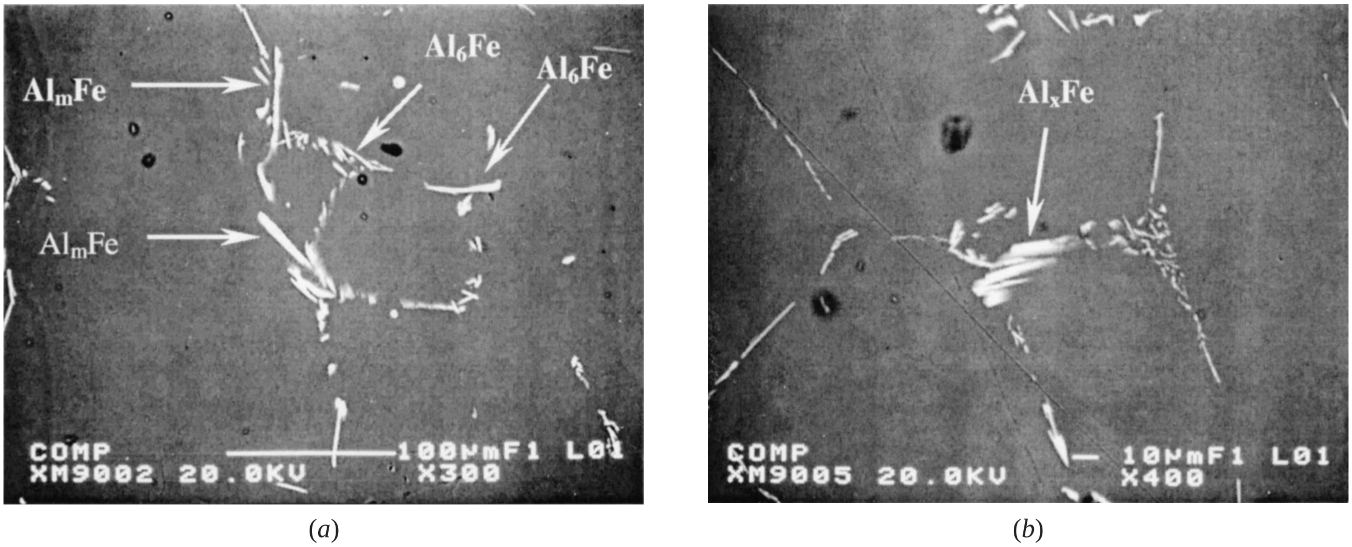

Fig. 8—(*a*) and (*b*) Backscattered images showing the iron intermetallics in the graphite mold-cast alloy 1 sample (cooling rate 0.16 °C/s).

metastable Al-Fe binary phases and destabilizes the Al_3Fe phase at slow cooling rates.

When alloy 1 was cast in the metallic mold (cooling rate, 10.7 °C/s), the δ- and β-AlFeSi ternary phases were observed to form. The size of these phases was not large enough compared to the size of the electron beam of the microanalyzer used to identify them. Consequently, due to contamination from the surrounding matrix, chemical analysis showed a higher aluminum content than expected. For this reason, the ratio Fe/Si has been used for identification of phases in almost all the rapidly cooled samples in this study.

It is also worth noting in Figure 8 that the binary Al-Fe phases are formed in the interdendritic regions. The formation of these high-Fe phases (26 to 33 wt pct Fe) in a dilute alloy (which contained 0.23 wt pct Fe) indicates that as solidification proceeded, the liquid phase was enriched with Fe, resulting finally in very rich interdendritic liquid regions from which the iron-rich phases could precipitate.

Thermal analysis of alloy 1 was carried out for both conditions of solidification (metallic and graphite molds). In the case the of graphite mold (Figure 9(a)), the cooling curve, first derivative, and corresponding temperature differences between the wall and the center thermocouples ($T_w - T_c$) are plotted. Two reactions can be distinguished: formation of the α-Al dendrites and precipitation of Al_6Fe through a eutectic reaction.[3] On the other hand, as a result of the high cooling rate (*i.e.*, very short solidification time, 3.9 seconds, and, hence, low volume fraction of intermetallics formed (Figure 6)), no thermal arrests apart from the development of the aluminum dendritic network were distinguished in the case of the metallic mold (Figure 9(b)). The solidification range being still wide (42 °C), the formation reactions of these phases had small heat effects. Thus, no noticeable peaks in the first derivative curve could be observed, because of the high rate of heat extraction during solidification in the metallic mold. Unlike the microstructure of alloy 1, which contained only binary Al-Fe intermetallic phases, alloy 2 contained no binary phases, as discussed in Section B.

B. *Alloy 2 (0.23 Pct Fe + 0.49 Pct Si)*

The data obtained from WDS analysis of the alloy 2 sample are also listed in Table II. The α-AlFeSi phase with its characteristic dendritic or Chinese script-like morphology is formed during slow cooling. The average composition of the phase was 27.4 wt pct Fe and 7.6 wt pct Si. In addition, some traces of Cu and Mn were found in this phase. As the composition of alloy 2 differs from that of alloy 1 only in its higher Si content, this leads to the conclusion that a Si content greater than 0.35 wt pct stabilizes the α phase. In contrast, the high cooling rate of the metallic mold promoted the formation of other phases, such as the β, δ, and q_1 AlFeSi phases, which were generally distinguished by their higher silicon contents. As Figure 10 shows, the collective morphology of these phases is featherlike and dendritic-like.

The α-AlFeSi phase displayed a noticeable thermal arrest in the cooling curve of alloy 2 cast in the graphite mold (Figure 11). The temperature of formation range was 633 °C to 611 °C, with a peak at 624 °C. Unlike the α phase, the heats of formation of the β and q_1 AlFeSi phases observed in the metallic mold-cast sample of alloy 2 were too weak to be detected, due to (a) the very short period of time over which these phases formed, (b) their very small volume fractions, and (c) the high rate of heat extraction of the metallic mold. The exception was the δ phase. It formed in the temperature range 600 °C to 611 °C, with a reaction peak at 604 °C and a very short time of formation, 0.3 seconds.

C. *Alloy 3 (0.55 Pct Fe + 0.62 Pct Si)*

The graphite mold-cast structure of alloy 3 contained α-AlFeSi and Si-rich spheroids, as shown in Figure 12. The chemical composition of the α-AlFeSi phase lies in the same range as that observed in alloy 2 (Table II). The Si-rich spheroid is probably a liquid inclusion. At the high cooling rate, both α- and δ-AlFeSi phases were observed to form (not shown). The corresponding cooling curve (Figure 13) shows that the thermal arrest of the α-AlFeSi phase is similar to that observed for alloy 2 when cooled slowly (Figure 11).

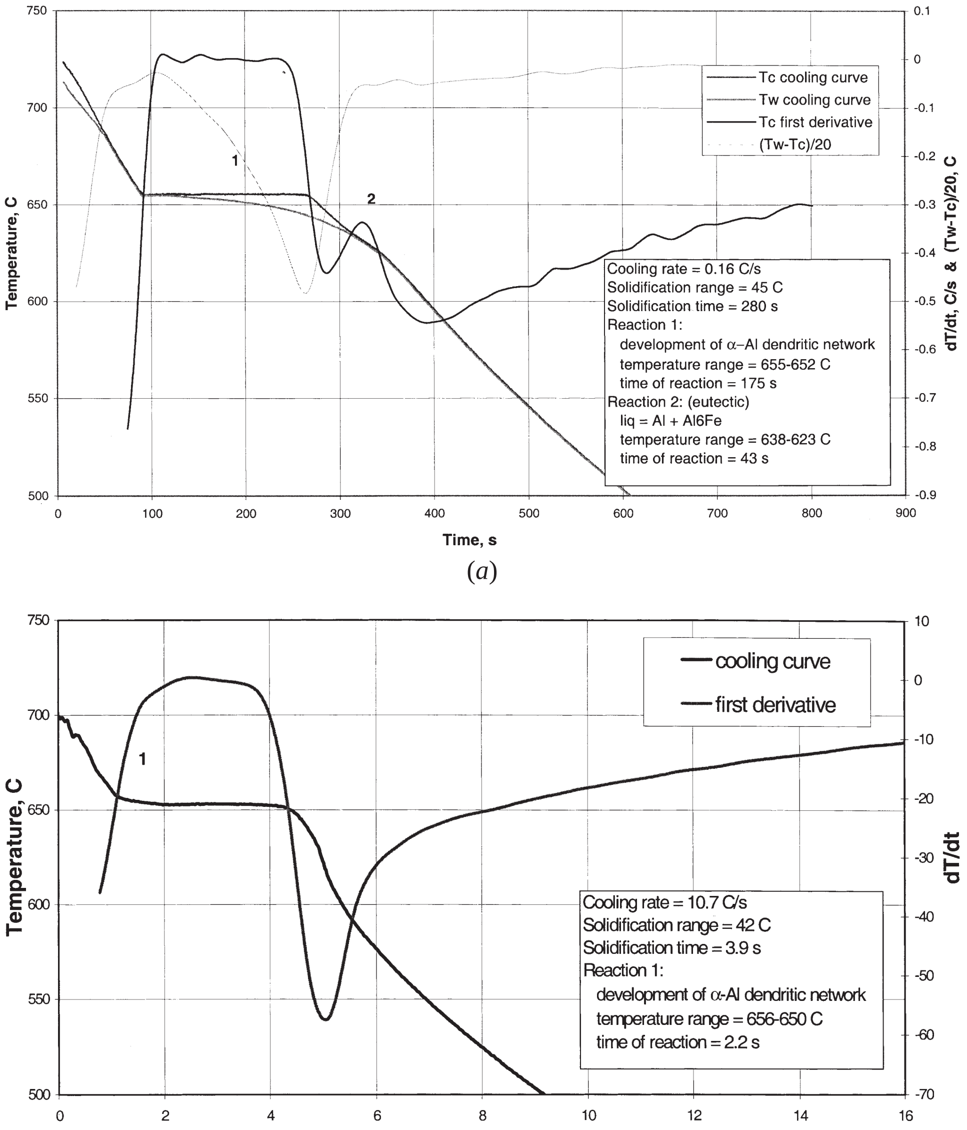

(*a*)

(*b*)

Fig. 9—Plots of thermal analysis data obtained for alloy 1 solidified in (*a*) graphite and (*b*) metallic molds. *Tc*: temperature corresponding to thermocouple at center of the mold, and *Tw*: temperature corresponding to thermocouple near the wall of the mold.

From Figure 13, the temperature of formation range of the α-AlFeSi phase was 631 °C to 615 °C, with the reaction taking 40 seconds. Apparently, the α-AlFeSi phase has a high latent heat of formation. On the other hand, well-defined peaks of two reactions corresponding to the formation of α and δ phases were identified from the thermal analysis curve of alloy 3 cooled in the metallic mold (Figure 13). The first reaction took place between 635 °C and 625 °C, with a temperature peak at 630 °C, corresponding to the formation of the α phase. The other reaction occurred between 617 °C and 609 °C, and reached a maximum at 612 °C, corresponding to the formation of δ-AlFeSi.

D. *Alloy 4 (0.56 Pct Fe + 0.90 Pct Si)*

The microstructure of alloy 4 obtained from the graphite mold casting contained both β- and α-AlFeSi phases (Table II), the two major iron intermetallic phases that form in commercial aluminum alloys. The average composition of the β phase was 60.7 wt pct Al, 26.4 wt pct Fe, and 14.1 wt pct Si (in addition to some trace elements of Cu, Mn, and Cr), corresponding to a formula of $Al_{4.75}FeSi$, which lies between those reported previously by Phillips[8] ($Al_9Fe_2Si_2$) and Mondolfo[30] (Al_5FeSi). The α-AlFeSi phase was observed more frequently than the β-AlFeSi phase in alloy 4. The chemical composition of the α phase corresponded to 62.7 wt pct Al, 30.2 wt pct Fe, 8.4 wt pct Si, and 0.5 wt pct Cu with traces of Mn and Cr. The α phase shows some variations in chemical composition, as is clear from a comparison of its compositions in alloys 2 and 3. Backerud *et al.*[27] have suggested that if Cu partially substitutes for Al, and Mn for Fe, the formula $(Al + Cu)_x(Fe + Mn)_ySi$ may be proposed, where x and y represent the appropriate values. The β phase, on the other hand, undergoes negligible variation in composition and morphology; it dissolves less trace elements and retains its platelike morphology.

At the high cooling rate, only the δ phase forms (Table II). The δ-Al_4FeSi phase is the highest silicon-bearing phase in the Al-Si-Fe system. As can be seen from Figure 4, its morphology is needlelike. This phase was reported to have nearly equal weight percentages of iron and silicon.[6,30] Its melting temperature is 870 °C (a peritectic decomposition);[6,26] therefore, it is stable below this temperature.

The thermal analysis data for alloy 4 are presented in Figure 14. The α phase, formed through a eutectic reaction simultaneously with aluminum, has a dendritic-like morphology. The reaction took place in the temperature range 634 °C to 625 °C for a period of 38 seconds, with a maximum peak at 631.5 °C. At lower temperatures, 614 °C to 600 °C, the β phase formed through peritectic decomposition of α-AlFeSi. This reaction has its maximum at 610 °C. The formation of δ-phase takes place at 621 °C to 611 °C. No other phase was observed in the microstructure except the δ phase, and it showed some variation in the Fe/Si atomic ratio. This variation is the result of the partial transformation of the δ phase to the β phase through the peritectic decomposition.[30]

$$\text{liq.} + \delta - Al_4FeSi_2 \rightarrow \beta - Al_5FeSi + Si$$

According to this reaction, the δ-phase particles start to transform into the β phase. Under conditions of high cooling rates and short solidification times, only very fine δ-phase particles can succeed in undergoing complete peritectic decomposition, because the reaction is totally controlled by the diffusion of silicon out of the δ phase (which is generally slow). In the case of large δ-phase particles, the reaction dies before completion, resulting in the formation of semi-decomposed/semiprecipitated δ-β, composite particles. These particles should contain a higher silicon content than the β phase, corresponding to their δ-phase roots. In addition, the microanalysis of these composite particles should rarely reveal a silicon level as low as that observed in the β phase (the condition of complete peritectic decomposition). Such particles composed of the δ phase in the core and β phase on the outside constituted the majority of particles that were selected for WDS microanalysis due to their relatively large sizes. This is evident from the chemical analysis of the δ phase (or δ-β composite particles) in alloys 1 through 4 listed in Table II.

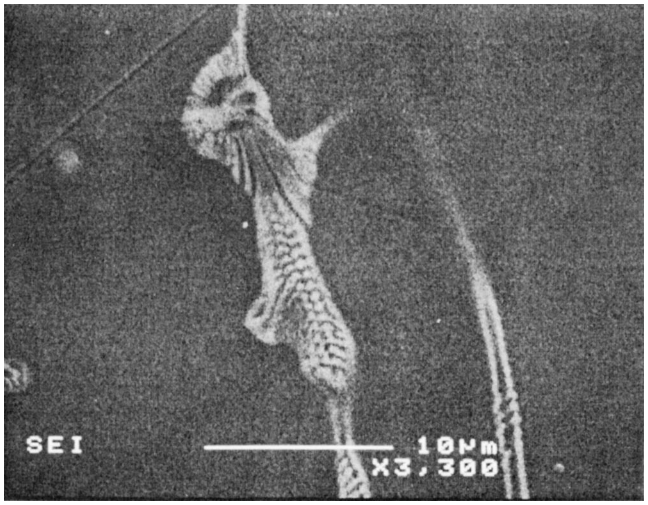

Fig. 10—Secondary electron image depicting the morphology of the iron intermetallics observed in the alloy 2 sample obtained from the metallic mold.

E. *Alloy 5 (1.03 Pct Fe + 0.62 Pct Si)*

Various iron intermetallic phases, both binary Al-Fe and ternary Al-Fe-Si, were observed to have formed in alloy 5 under the two conditions of solidification. It should be noted that alloy 5 contains the highest iron content among the six alloys studied. At the slow cooling rate (0.19 °C/s), the binary Al_mFe, Al_3Fe, and Al_6Fe phases are observed to precipitate. Their chemical compositions are listed in Table II. The chemical composition of the Al_mFe phase (32.2 wt pct Fe and 1.7 wt pct Si) corresponded to an m value of 4.25,

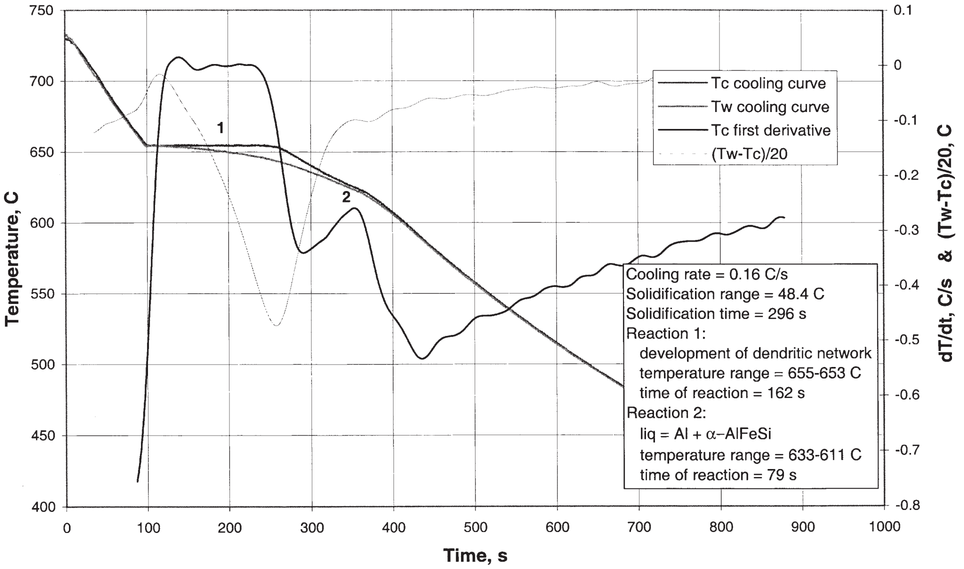

Fig. 11—Plot of thermal analysis data obtained for alloy 2 (Al-0.49 pct Si-0.23 pct Fe) solidified in the graphite mold.

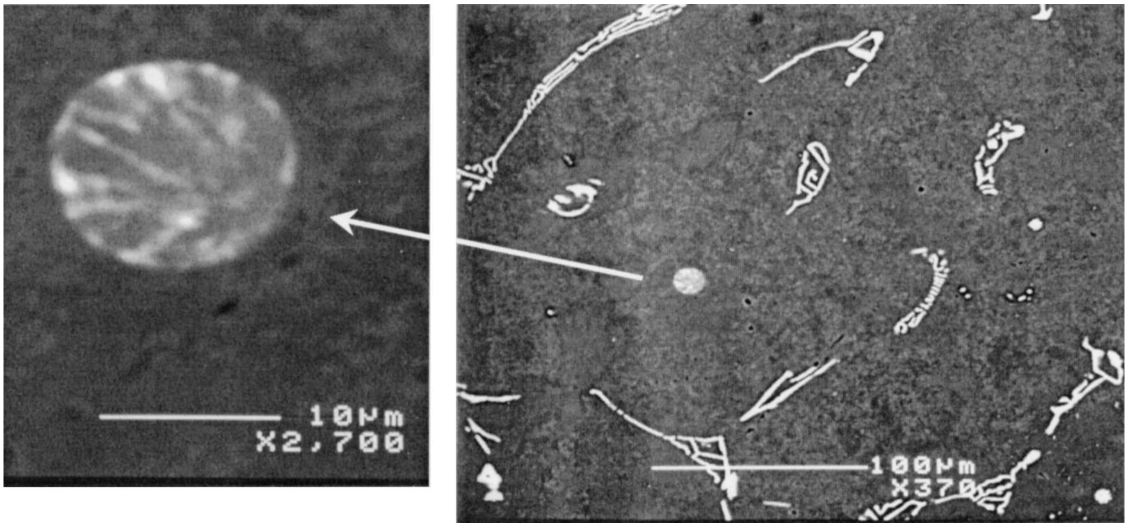

Fig. 12—Backscattered images obtained from the alloy 3 sample cast in the graphite mold. The image to the left shows a magnified view of the Si-rich spheroid particle.

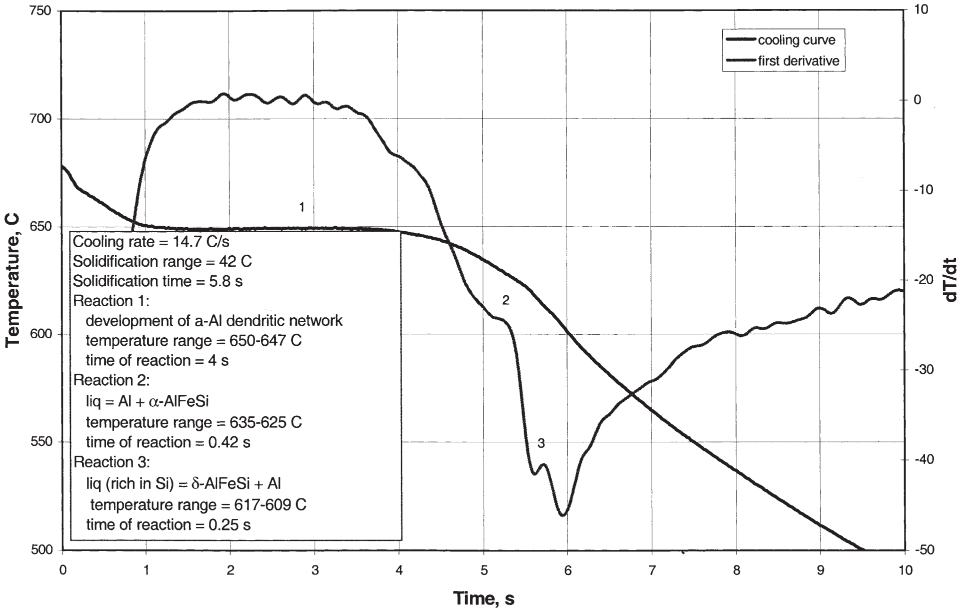

Fig. 13—Plot of thermal analysis data obtained for alloy 3 (Al-0.62 pct Si-0.55 pct Fe) solidified in the metallic mold.

which is higher than the *m* value obtained in alloy 1. The equilibrium phase, Al_3Fe, forms a eutectic with aluminum at about 652 °C. Its composition is 37.2 wt pct Fe and 1.5 wt pct Si, which gives a stoichiometry of $Al_{3.43}FeSi_{0.08}$. This formula lies in a composition range of $Al_{3.3-3.5}FeSi_{0.05}$, which was reported earlier by Dons.[31] On the other hand, the metastable Al_6Fe phase also forms a eutectic with aluminum,[3] the eutectic temperature being a few degrees lower than that of the Al-Al_3Fe eutectic.[27,32] The relation between the stable Al-Al_3Fe and the metastable Al-Al_6Fe systems resembles the well-known one between the stable Fe-C and metastable Fe-Fe_3C systems involved in the solidification of cast irons.[32] The iron content measured in Al_6Fe is similar to that found in alloy 1, *viz.*, ~26 wt pct, but its silicon content is higher, 1.8 wt pct (*cf.* 26.5 wt pct Fe in alloy 1). From these observations, we may conclude that the binary Al-Fe phases form only at slow cooling rates (0.16 °C/s to 0.19 °C/s) in low-Si alloys (*e.g.*, alloy 1 containing 0.35 wt pct Si) or high-Fe alloys (*e.g.*, alloy 5 with 1.03 wt pct Fe).

The α phase also precipitated under the same conditions and was observed more frequently in the microstructure. This leads to the conclusion that the composition of alloy 5 lies in the field of the Al + α + Al-Fe binary phases, and close to the boundary line of the α phase. The α phase has a composition of 29.2 wt pct Fe and 8.1 wt pct Si, with a stoichiometric formula of $Al_{9.2}Fe_2Si_{1.1}$. The Fe/Si atomic ratio measured in these particles was roughly

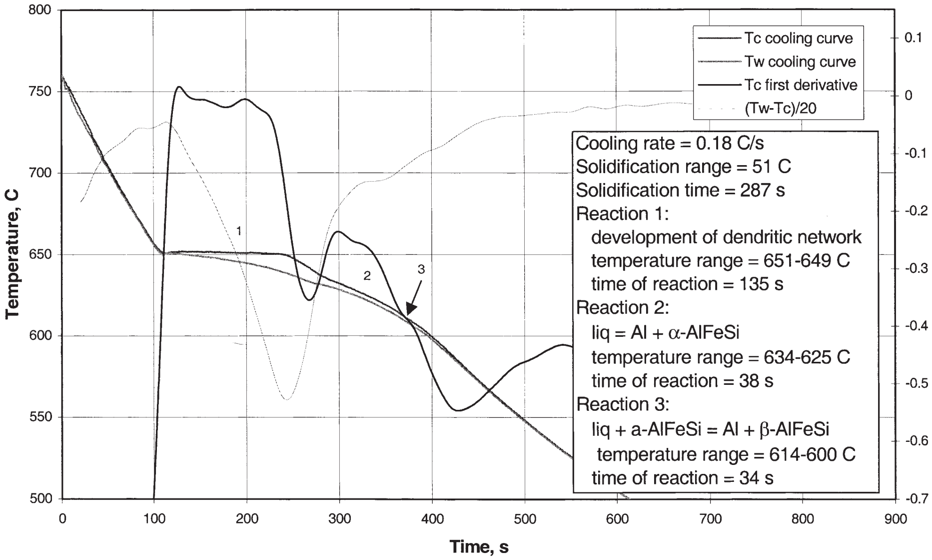

Fig. 14—Plot of thermal analysis data obtained for alloy 4 (Al-0.9 pct Si-0.56 pct Fe) solidified in the graphite mold.

the same as that found in the α-phase particles after rapid cooling (Table II).

The q_1-AlFeSi phase was composed of small, more or less rounded, particles that were arranged in featherlike or dendritic-like patterns (Figure 10). These particles contained 13 wt pct Fe and 4.3 wt pct Si, a composition similar to that of the q_1-phase particles observed in alloy 2, both conforming to the composition range reported recently by Liu and Dunlop.[33,34] For commercial purity alloy with a Fe/Si weight ratio of 2, these authors noted that the α-AlFeSi and q_1-AlFeSi phases dominated at high cooling rates, which corresponds exactly to our observations in the case of alloy 5 (Fe:Si $=$ 1.03:0.62) cooled in the metallic mold.

The Al_6Fe phase forms in the temperature range of 643 °C to 638 °C (for 18 seconds), as indicated by Reaction [2] in the thermal analysis curve of the alloy shown in Figure 15. The α-AlFeSi phase precipitates subsequently, between 630 °C and 618 °C for 34 seconds, followed by the Al_mFe phase, which occurs between 618 °C and 604 °C, for a duration of 43 seconds. Rapid cooling widened the range of α-phase formation to 629 °C to 611 °C (*cf.* 630 °C to 618 °C in the slowly cooled sample), but still maintaining the reaction peak at 625 °C. In addition, the q_1 phase formed between 590 °C and 570 °C, the reaction showing a weak heat effect and taking place over a long period of time (~3 seconds) when compared with the total solidification time, 6.8 seconds.

F. *Alloy 6 (0.52 Pct Fe + 6.32 Pct Si)*

The only iron intermetallic phase that was found in the microstructure of the graphite mold-cast alloy 6 sample was β-AlFeSi, with a composition of 56 wt pct Al, 26.8 wt pct Fe, and 14.8 wt pct Si, and containing some trace elements such as Cu, Mn, and Cr (Table II). This corresponded to a formula of $Al_{4.38}FeSi_{1.1}$, which is in good agreement with previous findings.[9,30] The lengths of the β-phase platelets observed in this case (an overall average of 15 μm, with certain platelets reaching up to 150 μm (Figure 16)) are longer than those found in other cases (Figure 6). This may be accounted for in part by the slow cooling rate and in part by the high Si content of the alloy. It is believed that the exceptional high stability of the β phase (equilibrium phase) within this region in the system also played a role.

The δ phase was the only iron intermetallic phase that was found in this alloy at high cooling rates (Table II). The phase was less distinguishable from the silicon particles (than, for example, the β phase) when viewed in the optical microscope/image analyzer system, due to their similar gray levels.

Because of its high silicon content (6.3 wt pct), the solidification range of alloy 6 is wide (82 °C). The solidification of the alloy at slow cooling rate, 0.18 °C/s, started with the development of the aluminum dendritic network (in the range 617 °C to 610 °C for 76 seconds). After that, the silicon eutectic reaction took place around 575 °C to 571 °C, lasting for a longer time (138 seconds) than the preceding or the succeeding reactions. Solidification ended with the final reaction corresponding to the formation of the β phase, which precipitated between 565 °C and 536 °C for about 102 seconds (Figure 17). The reaction of formation is a ternary eutectic reaction:

$$\text{liq. (rich in Fe and Si)} \rightarrow (\text{Al} + \text{Si}) + \beta\text{-AlFeSi}$$

The temperature range of this ternary eutectic reaction is relatively wide (565 °C to 536 °C, refer to the plot of thermal analysis data in Figure 17). This may be attributed to the smoothing schedule that was followed in order to make the chart more readable, which flattens the peaks of the first derivative. This effect may be very great, especially when the projection target curve (the cooling curve in this case) has a large slope. In addition, some trace elements such as Cu, Mn, and Cr were analyzed in the β needles. These elements might lower the eutectic temperature through the concurrent formation of their complex compounds very late at the end of solidification.

The interesting aspect of β-phase reaction is that, unlike the silicon eutectic temperature, which is only slightly affected

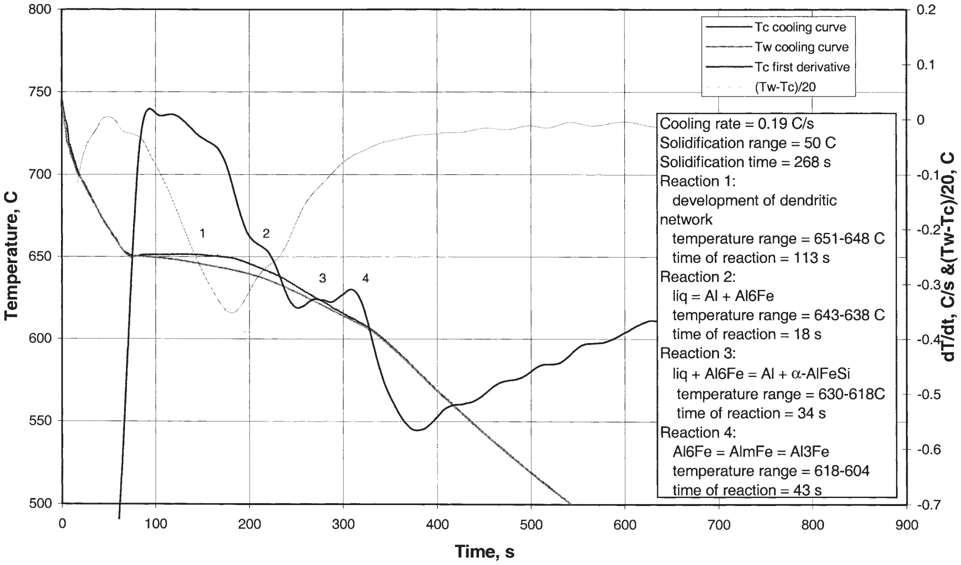

Fig. 15—Plot of thermal analysis data obtained for alloy 5 (Al-0.62 pct Si-1.03 pct Fe) solidified in the graphite mold.

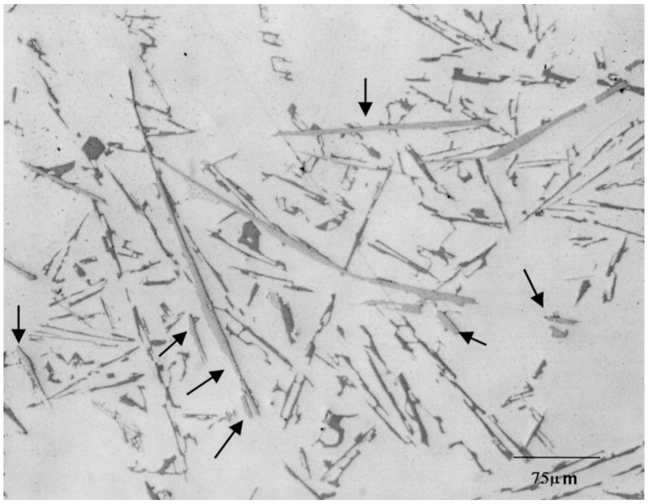

Fig. 16—Microstructure of alloy 6 obtained from graphite mold (cooling rate 0.18 °C/s). Arrows show the β-AlFeSi phase in the ternary eutectic Al-Si-β (short fine particles) and the primary β-AlFeSi phase (long platelets).

(less than 7 °C) by variations in cooling rate, the β-phase start temperature decreases with decreasing iron content, increasing cooling rate, and increasing melt superheat temperature until it eventually starts with the silicon eutectic temperature.[35,36,37] In the case of alloy 6, the silicon eutectic precipitates first and then the β-AlFeSi phase, as is clear from the thermal analysis data (Figure 17). However, for kinetic reasons, *i.e.*, difficulties to nucleate the silicon crystals (as a result of the purity and cleanliness of the alloy), some primary β-AlFeSi phases form before the start of the main eutectic reaction. This would explain the appearance of the evidently large β-AlFeSi platelets in the structure (Figure 16). A similar case occurred during the solidification of the high-purity alloy A356.2 and reported by Backerud *et al.*[27]

The formation of β-AlFeSi phase before the main eutectic is not highlighted in the sequence of solidification (Figure 17), because it is an exception that may or may not occur, depending on the purity of the alloy. In addition, no evidence was encountered for this reaction in the thermal analysis data.

The solidification range was observed to decrease from 82 °C at 0.18 °C/s to 61 °C at 12.8 °C/s cooling rate, owing to the fact that the δ phase precipitated as a proeutectic phase (610 °C to 603 °C), whereas it increased at the slow cooling rate, due to the precipitation of the β-AlFeSi as a posteutectic phase after the completion of Si precipitation. The difference in solidification range between the two cases was about 20 °C, which corresponds to the range of β-phase formation. Consequently, this would explain the formation of a high-Si phase such as δ-AlFeSi in the alloy at high cooling rates, because it precipitated from a Si-rich liquid. It would also explain the precipitation of the β-AlFeSi phase (with a relatively lower silicon content compared to the δ phase) during slow cooling, from the silicon-depleted liquid that remained after precipitation of silicon.

VII. EFFECT OF COOLING RATE

Cooling rate plays a basic role in stabilizing the different iron intermetallic phases in aluminum alloys, so that some phases are stabilized only at slow cooling rates, such as the binary Al-Fe phases, while others are stabilized at intermediate cooling rates, and still others, such as the δ-AlFeSi and q_1-AlFeSi phases, at only high cooling rates. There are also some phases, *e.g.*, α-AlFeSi, which have high stability over a wide range of cooling rates.

Slow cooling rates result in the formation of stable phases, while high cooling rates lead to the precipitation of metastable phases. The intermetallic phases that appear in a microstructure are controlled not only in terms of whether the cooling rate is high or low, but, more accurately, also by the fact that each of these phases is associated with certain cooling rate ranges. This fact is indispensable for a proper understanding of the alloy system. In view of this, some stud-

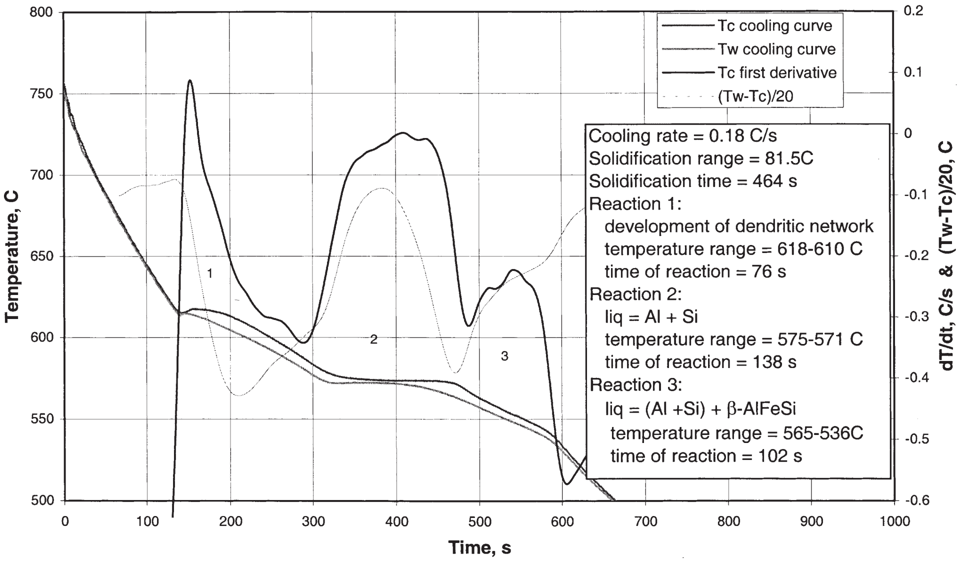

Fig. 17—Plot of thermal analysis data obtained for alloy 6 (Al-6.32 pct Si-0.52 pct Fe) solidified in graphite mold.

ies have specified the occurrence of Al-Fe binary phases to certain cooling rate ranges.[2,38] More recently, Young[3] has constructed cooling rate regimes for the formation of different intermetallic precipitates in hypoeutectic Al-Fe alloys. This problem was approached in part here by a thermal analysis study of the alloys investigated at different cooling rates.

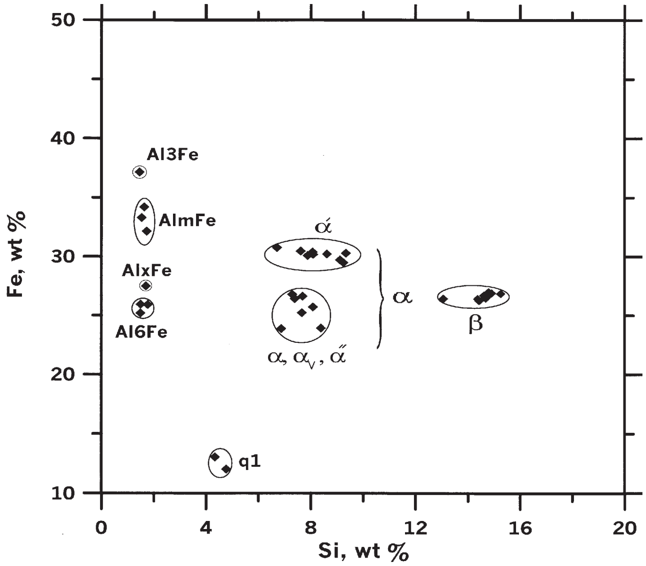

Fig. 18—Chemical composition diagram of the observed phases showing their ranges of homogeneity.

VIII. RANGE OF HOMOGENEITY

Some of the phases which were investigated in this study displayed a range of homogeneity. Their chemical compositions are summarized in Figure 18. Among all of the identified phases, α-AlFeSi has the widest range of homogeneity, a fact that was mentioned by Rilvin and Raynor in their review.[6] However, they did not distinguish between the different types of α-AlFeSi that have close chemical compositions but different crystal structures. Figure 18 shows that there are two phase chemistries that are classified generally as the α-AlFeSi phase, and both have the dendritic-like (Chinese script) morphology. At the same time, their chemical compositions lie close to each other within the range of occurrence of the α phase. The first type is designated α'—the phase referred to repeatedly in the literature as Al_8Fe_2Si, after the formula was accepted by Mondolfo.[30] The α' phase has a hexagonal symmetry and was reported earlier with slight variations in stoichiometry such as $Al_{11.8}Fe_3Si_{1.7}$[39] (or $Al_{7.86}Fe_2Si_{1.13}$) and $Al_{8\text{–}8.4}Fe_2Si_{1.06\text{–}1.33}$.[31] In the present work, the chemical composition of this phase was 29.48 to 30.75 wt pct Fe and 6.71 to 9.34 wt pct Si, exhibiting a larger range of homogeneity in silicon than in iron. The corresponding formula is expressed as $Al_{8.1\text{–}9.1}Fe_2Si_{0.87\text{–}1.25}$, covering a wider range of homogeneity than mentioned previously in the literature.[31,39]

The second type of the scriptlike α phase has a lower iron content, between 23.88 and 26.79 wt pct, a silicon content lying between 6.87 and 8.38 wt pct, and a chemical formula of $Al_{10.42\text{–}11.67}Fe_2Si_{1.08\text{–}1.25}$, which may be accepted as corresponding to the α phase (cubic crystal structure), the α_v phase with a monoclinic symmetry,[40] or the α'' phase with a tetragonal symmetry, because all three phases have a very close composition range. Regardless of the crystal symmetry of the phase, the phase displays a range of homogeneity in both of its iron and silicon contents.

The β-AlFeSi phase has a range of homogeneity as well (Figure 18), expressed by the formula $Al_{4.25\text{–}4.98}FeSi_{0.98\text{–}1.14}$. Almost all of the β-phase particles investigated in our study had iron contents ranging between 26 and 27 wt pct and silicon between 13 and 15 wt pct. This was the case for the ternary phases. Among the binary Al-Fe phases, it appeared that Al_mFe had a small range of homogeneity, as seen from the formulas $Al_{4.25}Fe$ (in alloy 5) and Al_4Fe (in alloy 1). The Al_6Fe is most likely a "point phase," as defined by Ferro and Saccone,[41] *i.e.*, a stoichiometric phase.

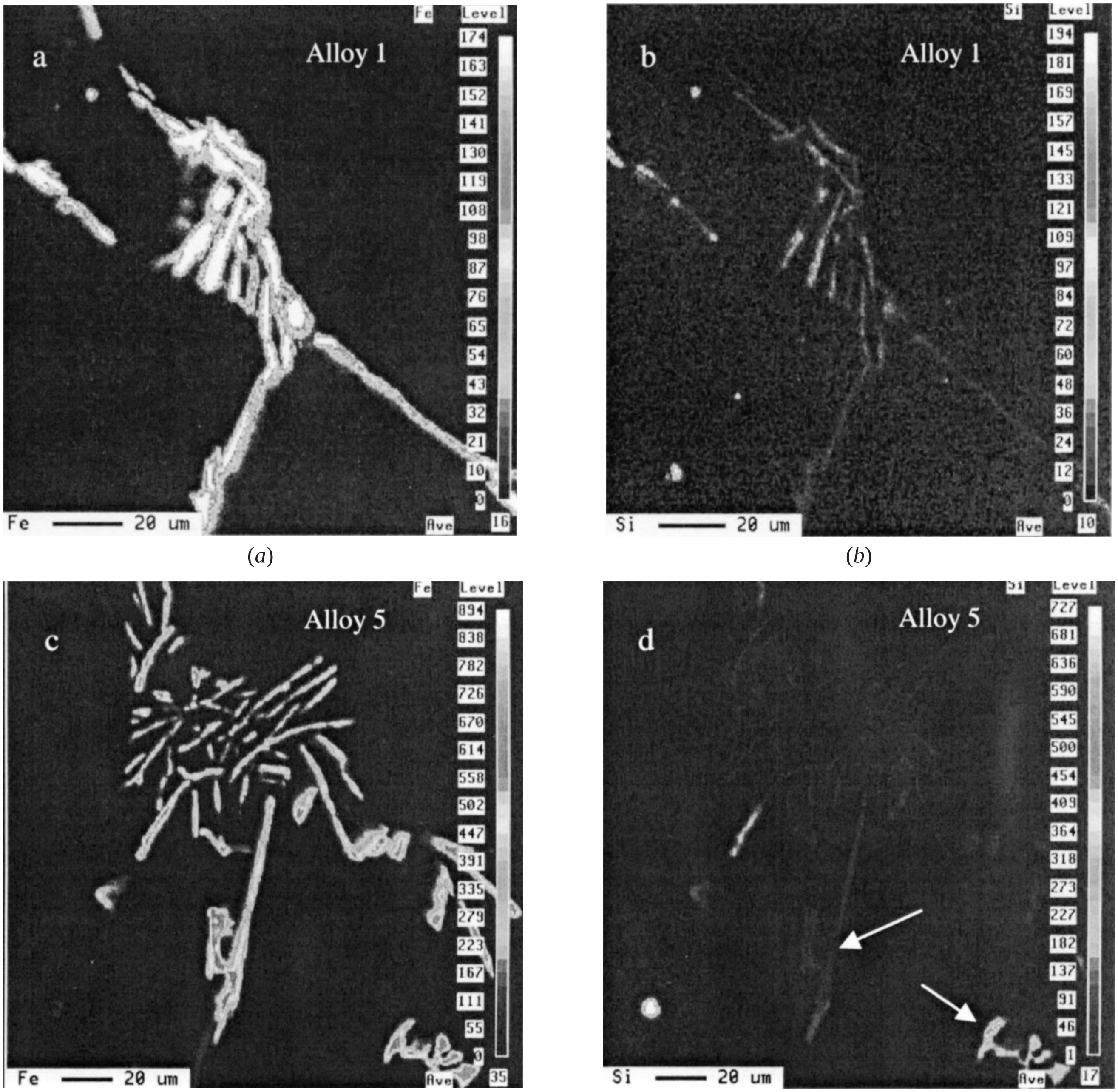

(*a*) (*b*)

(*c*) (*d*)

Fig. 19—Maps of Fe and Si element distributions observed in the microstructures of (*a*) and (*b*) alloy 1 and (*c*) and (*d*) alloy 5 samples obtained from graphite mold castings (~0.2 °C/s). Arrows in (*d*) delineate the presence of α-AlFeSi ternary phase diagram.

It should be mentioned here that the number of particles corresponding to other phases that were observed in the present work were insufficient to calculate their ranges of homogeneity.

IX. SILICON IN BINARY PHASES

All the binary Al-Fe phases observed in this study contained silicon levels between 1.48 and 1.76 wt pct. The silicon is most probably dissolved in the solid solution of these phases. Figure 19 shows maps of the iron and silicon distributions taken from the polished surfaces of the graphite mold cast samples corresponding to alloys 1 and 5. Alloy 1 contained only Al_mFe, Al_6Fe, and Al_xFe phases. These phases are seen to contain the highest iron levels in the field. In addition, it is obvious that all phase particles contain higher silicon levels than the matrix. This observation supports the WDS analysis shown in Table II. Although the binary Al-Fe particles in alloy 5 are similar to those seen in alloy 1, the microstructure of alloy 5 also displayed α-phase particles that possessed a higher silicon content than the binary phases and the matrix (arrows).

X. MICROSEGREGATION OF IRON AND SILICON DURING SOLIDIFICATION

Microsegregation is an inevitable result of solidification. As long as the partition coefficient of the solute atoms in

Table III. Iron and Silicon Contents in the Aluminum Matrix of Different Alloys

Alloy	Cooling Rate, C/s	Si, Wt Pct	Fe, Wt Pct
3	14.7	0.24	0.051
4	12.8	0.18	0.049
5	14.3	0.60	0.103
5	0.19	0.28	0.043
6	12.8	1.43	0.034

the alloy is equal to a value other than unity, microsegregation would result. The equilibrium partition coefficients of Si and Fe in aluminum are 0.14 and 0.022, respectively. In addition, these were confirmed to be almost constants in the temperature range of 570 °C to 620 °C in the alloy 356.[42] Thus, successive enrichment of the liquid phase in these elements is expected to occur during crystal growth.

The iron and silicon contents measured in the matrix are listed in Table III. The iron concentration in the matrices of alloys 3 and 4 obtained at a high cooling rate reached its solubility limit in aluminum, which is 0.05 pct. In alloy 5, however, this value doubled to 0.103 wt pct Fe in the matrix (at high cooling rate). At the same time, the Si content increased sharply to 0.6 wt pct, a value much higher than those determined in alloys 3 and 4. In contrast, the iron level in the matrix of alloy 5 decreased to 0.043 wt pct (lower than the solubility limit) at slow cooling rate. It can also be seen from Table III that, in alloy 6, silicon builds up to 1.43 wt pct in the matrix, a value that is close to its solubility limit in aluminum (1.6 wt pct at 577 °C).[43]

The behavior of iron and silicon in the aluminum matrix and the formation of Fe- and Si-rich phases can be explained using the theory of solidification and the available diffusion data. The diffusion coefficients of silicon and iron in aluminum were determined by extrapolation of the diffusion coefficient-temperature diagram compiled by Hatch.[26] It can be observed from this diagram that the diffusion coefficient of silicon in aluminum is much higher than that of iron in aluminum (about 10^4 times higher, in the temperature range 500 °C to 650 °C). At 650 °C, the diffusion coefficients are 10^{-7} and 10^{-11} cm^2/s for silicon and iron, respectively. In addition, the diffusion coefficient of silicon in aluminum is also higher than that of aluminum. In spite of the fact that these data were measured in the solid state, they are still valuable in that they indicate, qualitatively at least, that the diffusion of silicon in aluminum takes place much more easily than that of iron.

Diffusion during the process of crystal growth plays an important role. It affects, in part, the solute redistribution between solid and liquid, causing the production of a microsegregated structure. The well-known nonequilibrium lever rule or Scheil equation is usually used to describe solute redistribution in crystal growth processes. The Scheil concept supposes no solid diffusion and complete liquid diffusion. Applying the Scheil equation, calculations tracing the liquid composition as a function of solid fraction (solidification paths) were made. In these calculations, it was assumed that (1) there is no chemical interference between iron and silicon before they start to form intermetallic particles, and (2) there is no physical interaction that can affect the solubility of either species (Fe or Si) in aluminum. The results were plotted on the liquidus projection of the system (Figure 20).

As can be seen from the figure, the Scheil equation gives a poor estimation with regard to iron segregation. It overestimates the iron segregation to the liquid phase, leading to wrong estimations of the solidification sequence. Consequently, the segregation paths for five out of the six alloys are seen to intersect with the boundary line of the binary Al_3Fe phase, suggesting the formation of binary Al-Fe phases. Actually, only alloys 1 and 5 were observed to contain binary phases in their microstructures, as confirmed by the thermal analysis and element distribution mappings that were carried out for these alloys.

The precipitation behavior in the case of the other alloys (2, 3, and 4) was also quite different from that expected from the Scheil approximation. In the case of alloy 6, the Scheil segregation path intersected with the boundary line of β-AlFeSi, thus estimating the formation of the β phase first. To the contrary, and according to the actual sequence, the formation of the binary Al-Si eutectic took place before the precipitation of the β phase.

The assumption made by the Scheil equation that no solid diffusion takes place essentially implies that the calculations are made without taking into consideration any diffusion parameters. In view of the fact that the relatively easy diffusion of Si in aluminum compared to Fe has not been considered, this omission would explain in general why the actual solidification paths deviate from the Scheil approximations for almost all of the alloys in this study.

In view of these results, trials to calculate solidification paths to account for the departures from the Scheil behavior were made according to the models of Brody and Flemings[44] and Clyne and Kurz.[45] The first model assumes that the concentration gradient in the solid is constant, while the second one assumes that the concentration gradient in the solid at the end of solidification is very high, and, therefore, the driving force for diffusion is also considerably high.

According to Brody and Flemings,[44] the extent of back-diffusion taking place in the solid phase during solidification depends on a dimensionless parameter α (given by $\alpha = D_s/RL$),[1,44] where D_s is the solid-diffusion coefficient at the melting point, R (given by L/t_f) is the local interface velocity, L is half of the dendrite arm spacing, and t_f is the local solidification time in the unit volume. The value of t_f is not known, so we assume the velocity of the interface R by dividing the radius of the sample by the solidification time, which gives $R = 3$ cm/300 s $= 10^{-2}$ cm/s. The average dendrite arm spacing is about 100 μm in our alloys ($L = 100/2 = 50$ μm).

This parameter can be regarded as describing the ratio of the diffusion boundary layer in the solid to the size of the unit volume, L. The larger the value of α, the more significant the role of solid diffusion in solute redistribution according to the equation:

$$C_L = C_0\left(1 - \frac{f_s}{1 + \alpha k}\right)^{k-1} \qquad [1]$$

where k is the partition coefficient, f_s is the solid fraction, C_L is the liquid composition, C_0 is the initial composition of the alloy. Substituting the corresponding values of D_s and k and taking $R = 10^{-2}$ cm/s and $L = 50$ μm results

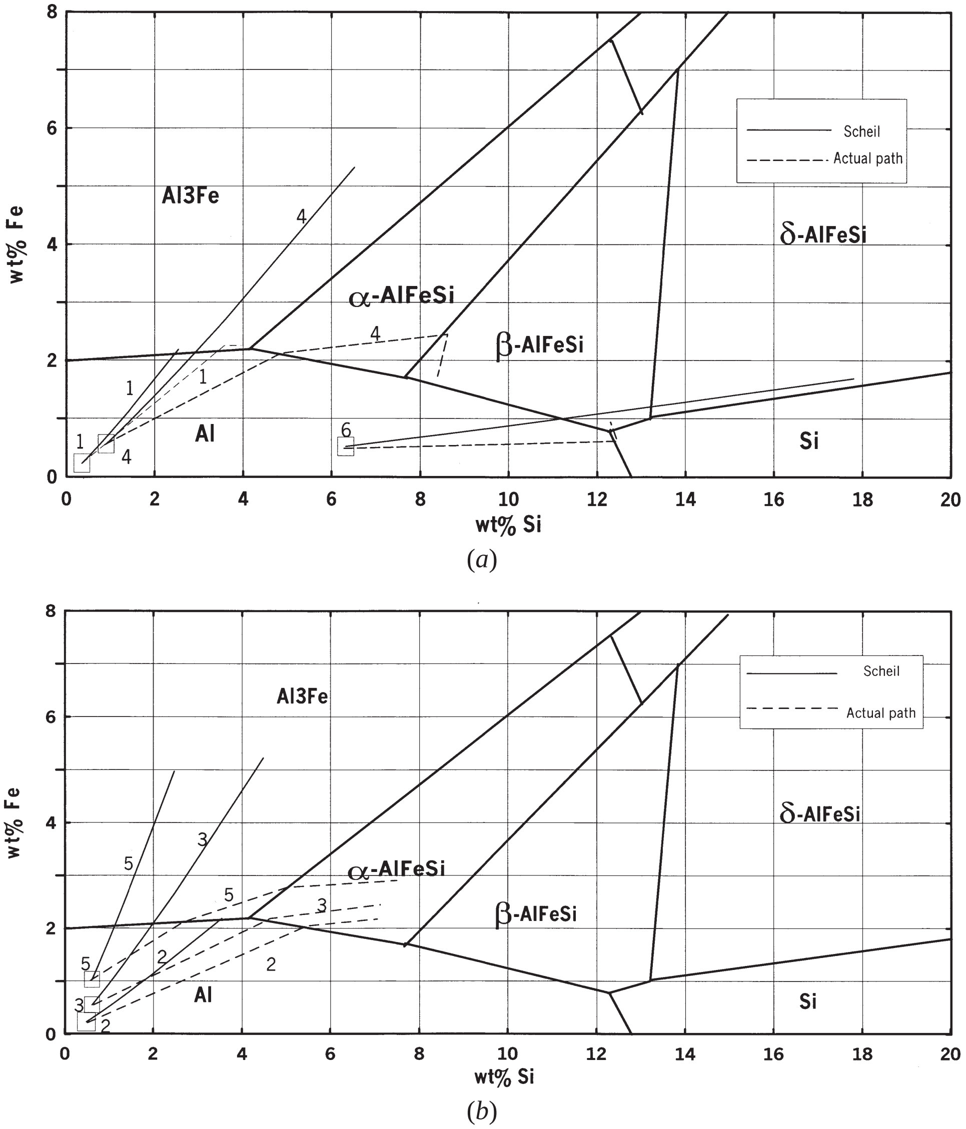

(*a*)

(*b*)

Fig. 20—(*a*) Solidification paths for alloys 1, 4, and 6 according to the Scheil equation compared with the actual paths. The squares marked 1, 4, and 6 denote the respective alloy compositions. (*b*) Solidification paths for alloys 2, 3, and 5 according to the Scheil equation compared with the actual paths. The squares marked 2, 3, and 5 denote the respective alloy compositions.

in α values of 2×10^{-7} and 2×10^{-3} for iron and silicon, respectively. The very small values of the parameter α indicate that solid-diffusion (back-diffusion) of silicon and iron are negligible according to this model, because the value of $(1 + \alpha K)$ in Eq. [1] is still equal to unity for both Fe and Si.

Clyne and Kurz[45] approached back-diffusion through a spline-smoothing function α', given by[45,46]

$$\alpha' = \alpha\left(1 - \exp\left(-\frac{1}{\alpha}\right)\right) - \frac{1}{2}\exp\left(-\frac{1}{2\alpha}\right) \qquad [2]$$

This function introduces the effect of back-diffusion when α' replaces α in the segregation equation:

$$C_L = C_0(1 - (1 - 2\alpha k)f_s)^{(k-1)/(1-2\alpha k)} \qquad [3]$$

Substituting our values for the parameters in this relation leads to the Scheil behavior, as the α' values are reduced to α values for both iron and silicon. Thus, both of these models essentially revert to the Scheil behavior, because they give much less weight to the effect of solid diffusion. In addition, the low solid-state diffusivities of iron and silicon also play a role. These diffusivities are low because of the substitutional nature of the diffusion of iron and silicon in aluminum (atomic radii of iron and silicon are close to that of aluminum, 1.72, 1.46, and 1.82 Å, respectively.)

Although the theoretical models of Brody and Flemings[44] and Clyne and Kurz[45] cannot account for the deviation from Scheil behavior observed in our study, the experimental results of Potard *et al.*[47] support our proposal that these theoretical models give less weight to the effect of solid-state back-diffusion than they should. Potard *et al.*, based on their work, reported that impurity distribution in aluminum (including iron) is influenced by its speed of diffusion in the solid phase. They also reported that iron diffusion is very difficult and that the diffusion coefficient is independent of the Fe concentration.

The departure from the Scheil equation also arises from the assumption that there is no interaction or interference between the diffusing species considered for simplifying the calculation of the solidification paths. Mondolfo[30] stated that iron does not appreciably affect the diffusion of other metals in aluminum. In contrast to the effect of iron, the activation energy for the diffusion of iron dissolved in aluminum is lowered by silicon: from a value of 1.65 eV for a pure Al-Fe alloy to a value of 1.35 eV with an addition of 0.12 pct Si. Miki and Warlimont[48] reported that silicon increases the Al_3Fe precipitation rate by lowering the activation energy for iron diffusion in solid aluminum.

These data[30,48] show that the diffusion of silicon is not affected by the presence of iron, whereas the diffusion of iron requires less energy and, therefore, becomes easier, in the presence of silicon. Consequently, the easier diffusion of iron in the solid phase in the presence of silicon would result in a more even distribution of the iron by lowering the concentration gradient in the solid close to the solid/liquid (S/L) interface. This, in turn, would lead to a lower iron concentration on the solid side of the S/L interface. According to the theory of solidification, which postulates equilibrium at the S/L interface, this would necessitate a lower iron concentration on the liquid side of the interface, leading to less iron buildup in the liquid phase. If local equilibrium at the S/L interface does not persist, constitutional supercooling of the liquid in front of the interface will result, as is the case in dendritic growth.

In dendritic growth, the prediction of the Scheil equation concerning microsegregation will not be exactly correct,[49] because the assumption of complete mixing in the liquid phase is not valid, as complete homogeneity in the liquid cannot be attained. The diffusion analysis carried out by Allen and Hunt,[49] however, suggests that the deviations from Scheil behavior may often be negligible except at high growth rates. Thus, the formation of a solute-rich layer in the liquid would not be noticeable, because either Scheil (complete mixing in the liquid) or near-Scheil conditions (negligible effect of incomplete mixing in the liquid as encountered in dendritic growth)[49] would persist throughout solidification. The condition of equilibrium (planar or cellular interface) or near-equilibrium (dendritic growth) at the S/L interface coupled with the enhanced diffusion of iron in the solid phase would result in lower iron segregation to the liquid, which would explain the departure of the actual solidification paths from the Scheil approximation shown in Figure 20. A schematic representation of these arguments is depicted in Figure 21.

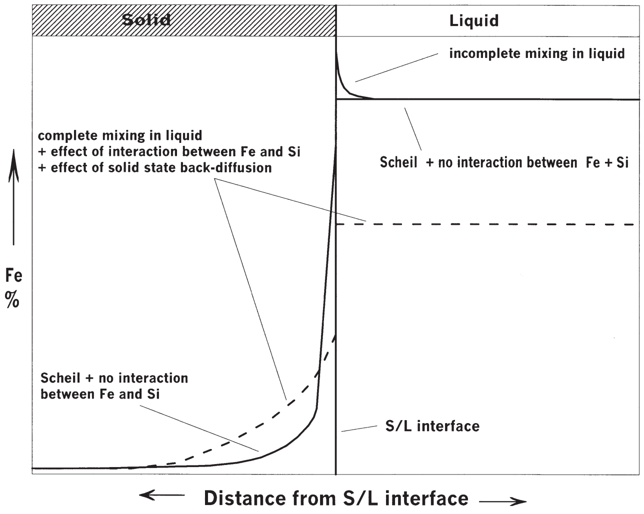

Fig. 21—Schematic diagram showing the effect of Fe-Si interaction on the iron distribution between solid and liquid alloy regions.

So far, we have discussed the situation when low cooling rates (which lead to slow growth rates) are dominant and have explained the departure from Scheil behavior that is observed in such cases. Now we shall consider what happens when high cooling rates are dominant, which are found to lead to the formation of Si-rich phases.

At fast growth rates, substantial departures from equilibrium at the S/L interface exist, so that solute concentrations far in excess of the equilibrium solid solubility limit are attained. This phenomenon rules out local equilibrium and the idea that major and minor components act independently at the interface during rapid solidification.[50] Furthermore, Aziz[50] has demonstrated that the transition from equilibrium solidification to complete solute trapping occurs as the velocity of the S/L interface surpasses the diffusion speed of solute in the liquid. Alloys 3 and 4 have the same iron content (0.55 wt pct), and on account of their short solidification times (5.8 and 3.9 seconds, respectively), when solidified in the 1-in.-diameter metallic mold, both of them achieve the same high iron level in the matrix (~0.05 wt pct), which corresponds to the limit of solid solubility. The amount of the entrapped element depends on the alloy content, as is clear from Table III, which indicates that more iron was entrapped in alloy 5 than in alloy 3 or 4. The entrapped silicon content in the matrix is relatively lower than that of iron, when considering their (Si, Fe) solid solubilities and the alloy compositions. In alloy 6, which contains 6.3 pct Si, the matrix contains 1.43 pct Si after rapid cooling. This can also be attributed to the higher diffusion coefficient of silicon in aluminum than that of iron.

Silicon solubility in aluminum is reduced with the increase in cooling rate.[30] As a result, the stability of phases changed. Thus, the reduced silicon solubility, coupled with the relatively small Si content entrapped in the solid phase at high cooling rates, can explain the formation of Si-rich phases such as the δ phase in alloys that lie far outside the boundary of the δ phase region in the equilibrium phase diagram. In addition to the δ phase, the alloy microstructures observed at high cooling rates were also characterized by the disappearance of the Al-Fe binary phases and the presence of ternary phases. Also, the high level of silicon content entrapped in alloy 5 matrix and, thereby, the depletion of Si in the liquid, explains why the δ phase was not observed in this alloy. On the other hand, at slow cooling rate, apart from the iron and silicon retained in the matrix (0.28 and 0.043 wt pct, respectively), the relatively high-Fe and low-Si contents of this alloy available in the interdendritic regions resulted in the formation of Fe-rich phases such as binary Al-Fe phases or high-Fe ternary Al-Fe-Si phases such as the α phase. In contrast to the supersaturation of iron in aluminum (alloy 5), due to the high diffusion coefficient of silicon in aluminum, silicon supersaturation of the matrix did not occur, even at high cooling rates and in the high-Si containing alloys (*viz.*, 6.3 wt pct in alloy 6).

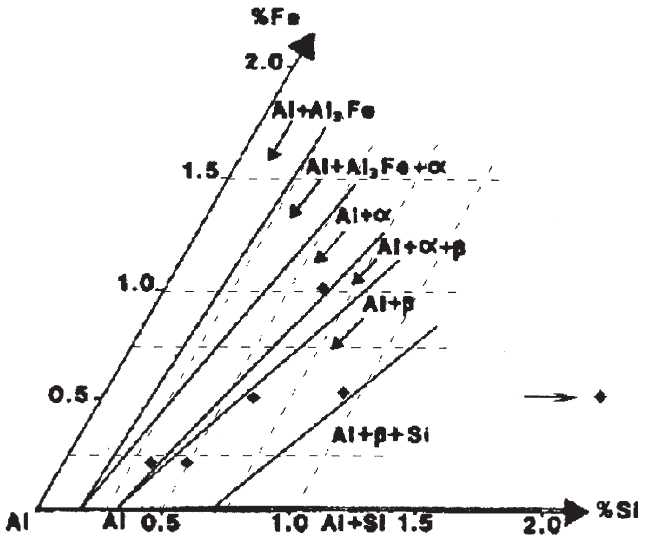

Fig. 22—Positions of the experimental alloys (1 through 6) on the 500 °C isothermal section for the Al corner of the Al-Si-Fe system.

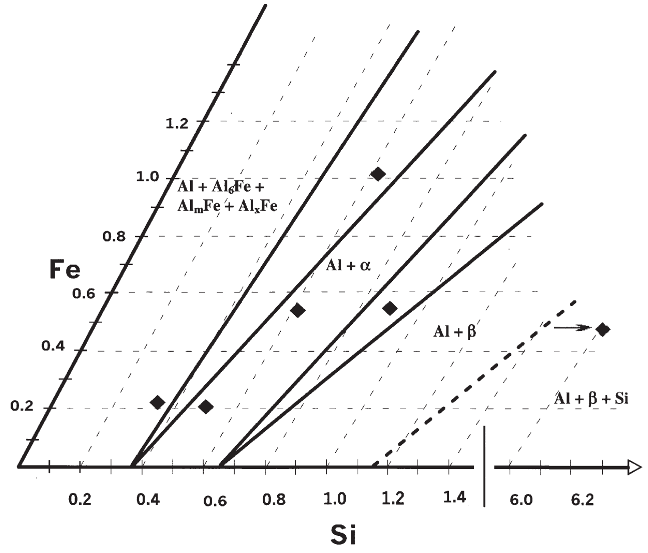

Fig. 23—Metastable section at the solidus temperature for the Al corner of the Al-Si-Fe system. The black squares denote the alloy compositions.

IX. PHASE DIAGRAM ADJUSTMENT

The isothermal section of the ternary phase diagram of Al-Si-Fe at 500 °C according to Philips[8] is shown in Figure 22. The 500 °C section is revised here, because all the reactions that take place during the solidification of our alloys end at temperatures higher than 500 °C. The positions of the six experimental alloys of our study are marked on the diagram. Comparing these positions with the diagram predictions, it is evident that the Philips diagram cannot be used to predict the phases observed in alloys 1 through 5 after solidification at slow cooling rates (~0.2 °C/s, graphite mold). Similar observations were previously reported by Dons.[31]

An adjustment to the Philips isothermal section is proposed in Figure 23, where the phase boundaries have been shifted to the higher silicon side so as to conform to our experimental observations. The phase relations that appear in Figure 23 must be considered an approximation for the structure of the alloys after nonequilibrium cooling conditions. Thus, the diagram is termed "metastable section at the solidus temperature."

The phase boundary for silicon formation (the dashed line between Al + β and Al + β + Si fields), however, has been plotted according to the isothermal phase projections published in the ASM Specialty Handbook.[43] These adjustments allow correct phase predictions for all the alloys without exception. In comparison, while the new adjustments respect the sequence of phase fields given in the Philips diagram, each field now exists in a higher silicon range.

Figure 24 summarizes the intermetallic phases that were observed after solidification in the metallic mold (*i.e.*, at high cooling rate). It is clear that the δ phase was the phase most frequently identified in the microstructures of these alloys, and became the dominant phase at high silicon contents. The α phase was encountered in alloys containing relatively high iron and medium silicon levels (*viz.*, alloys with a relatively higher iron content compared to silicon), whereas the β phase precipitated at the lowest iron contents alloys (*i.e.*, in alloys whose Si levels were relatively higher that their Fe levels).

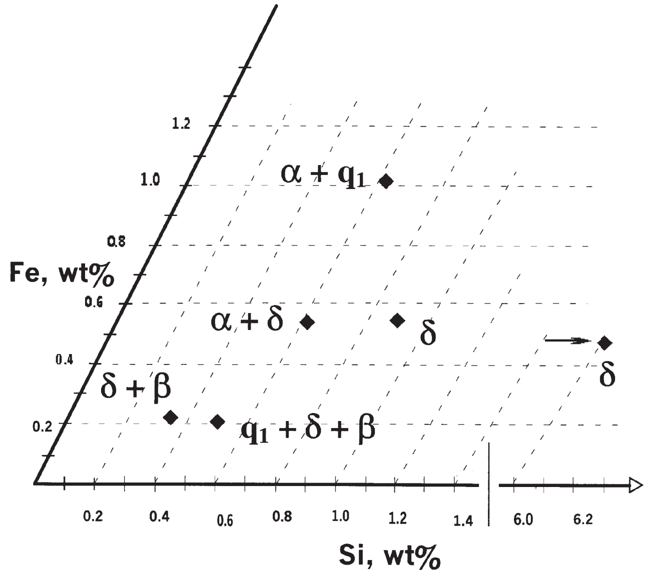

Fig. 24—Schematic diagram showing the intermetallic phases observed in the alloys studied, obtained at high cooling rate (0.16 °C/s to 0.2 °C/s, metallic mold).

X. SUMMARY

Optical microscopy, quantitative metallography, scanning electron microscopy, thermal analysis, microprobe analysis, and WDS were used to the study the iron intermetallic phases observed in six experimental dilute aluminum alloys at slow (0.16 °C/s to 0.21 °C/s, graphite mold) and high (10 °C to 15 °C/s, metallic mold) cooling rates. The volume fraction of iron intermetallic phases is higher in the former (slowly cooled samples) than the latter case. In both cases, the volume fraction increases as the alloying content of iron and silicon increases. However, the iron content is more effective in producing intermetallics than the Si or Fe + Si contents. The density of iron intermetallics is also higher at high cooling rates. In contrast, large-sized intermetallics are obtained at slow cooling rates.

Phase stability changes with cooling rate and alloy composition. Thus, binary Al-Fe phases form only at a slow cooling rate when Fe contents are higher relative to the Si content of the alloy. The β-AlFeSi phase dominates at high silicon levels and slow cooling rates. The α-AlFeSi phase field exists between the binary Al-Fe phases and the β phase. Rapid cooling stabilizes silicon-rich ternary phases such as the δ phase and diminishes the binary ones, because rapid cooling decreases the solubility of silicon in liquid aluminum and causes entrapment of iron in solid. The δ-AlFeSi phase is the dominating phase at 0.9 wt pct silicon and higher.

Solidification paths representing the segregation of iron and silicon to the liquid were calculated using the Scheil equation. The actual solidification paths did not conform to Scheil behavior, as less iron was observed to have segregated actually to the liquid than that estimated by the Scheil equation. The reason for this overestimation (of iron content in the liquid) is that the Scheil equation postulates that there is no solid diffusion. Similarly, the theoretical models of Brody and Flemings[44] and Clyne and Kurz[45] cannot explain the departure from Scheil behavior as they give much less weight to solid-state back-diffusion. It has been shown qualitatively that the interaction between iron and silicon (which facilitates the diffusion of iron in solid aluminum), together with the suggested role of more effective solid diffusion, could account for the departure from Scheil behavior.

An adjusted 500 °C metastable isothermal section of the Al-Si-Fe phase diagram has been proposed. The adjustments were made to the published equilibrium section in order to correctly predict the phases that are observed in this part of the system at slow cooling rates (0.2 °C/s).

ACKNOWLEDGMENTS

Financial support from the Natural Sciences and Engineering Research Council of Canada (NSERC), General Motors Powertrain Group, Corporative Nemak, and the Centre québécois de recherche et de développement de l'aluminium (CQRDA) is gratefully acknowledged. The authors also thank Mr. Glenn Poirier, Microanalysis Laboratory, Earth and Planetary Sciences, McGill University, for carrying out the WDS analysis.

REFERENCES

1. M.C. Flemings: *Solidification Processing*, McGraw-Hill, New York, NY, 1974.
2. I. Miki, H. Kosuge, and K. Nagahama: *Journal of Japan Institute of Light Metals*, 1975, vol. 25, pp. 1-9.
3. R.M. Young: *Scripta Metall.*, 1981, vol. 15, pp. 1211-16.
4. Y. Choi, J. Lee, W. Kim, and H. Ra: *J. Mater. Sci.*, 1999, vol. 34, pp. 2163-68.
5. H. Tanihata, T. Sugawara, K. Matsuda, and S. Ikeno: *J. Mater. Sci.*, 1999, vol. 34, pp. 1205-10.
6. V.G. Rilvin and G.V. Raynor: *Int. Metall. Rev.*, 1981, vol. 3, pp. 133-52.
7. D. Munson: *J. Inst. Met.*, 1967, vol. 95, pp. 217-19.
8. H.W. Philips: *Annotated Equilibrium Diagrams of Some Aluminum Alloy Systems*, The Institute of Metals, London, 1976.
9. V. Stefaniay, A. Griger, and T. Turmezey: *J. Mater. Sci.*, 1987, vol. 22, pp. 539-46.
10. C.Y. Sun and Mondolfo: *J. Inst. Met.*, 1967, vol. 95, p. 384.
11. P.J. Black: *Acta Cryst.*, 1955, vol. 8, pp. 43-48.
12. H. Suzuki and M. Kanno: *Journal of Japan Institute of Light Metals*, 1978, vol. 28, pp. 558-65.
13. L.K. Walford: *Acta Cryst.*, 1965, vol. 18, pp. 287-91.
14. D. Porter and H. Westengen: *Quantitative Microanalysis with High Spatial Resolution*, TMS, Warrendale, PA, 1981, pp. 94-100.
15. H. Kosuge and I. Mizukami: *Journal of Japan Institute of Light Metals*, 1972, vol. 22, pp. 437-44.
16. S. Asami, T. Tanaka, and A. Hideno: *Journal of Japan Institute of Light Metals*, 1978, vol. 28, pp. 321-27.
17. H. Westengen: *Z. Metallkd*, 1982, vol. 73, pp. 360-68.
18. E.H. Hoolingsworth, G.R. Frank, and R.E. Willett: *Trans. AIME*, 1962, vol. 224, pp. 188-89.
19. R.C. Hudd and W.H. Taylor: *Acta Cryst.*, 1962, vol. 15, pp. 441-42.
20. K. Robinson and P.J. Black: *Phil. Mag.*, 1953, vol. 44, pp. 1392-97.
21. M. Cooper: *Acta Cryst.*, 1967, vol. 23, 1106-07.
22. A.L. Dons: *Z. Metallkd.*, 1985, vol. 76, pp. 151-58.
23. P. Skjerpe: *Acta Cryst.*, 1988, vol. B44, pp. 480-86.
24. J. Gjonnes, V. Hansen, B. Berg, P. Runde, Y. Cheng, K. Gjonnes, D. Dorset, and C. Gilmore: *Acta Cryst.*, 1998, vol. A54, pp. 306-19.
25. L. Narayanan, F.H. Samuel, and J.E. Gruzleski: *Metall. Mater. Trans. A*, 1994, vol. 25A, pp. 1761-73.
26. J. Hatch: *Aluminum, Properties and Physical Metallurgy*, ASM, Metals Park, OH, 1984.
27. L. Backerud, G. Chai, and J. Tamminen: *Solidification Characteristics of Aluminum Alloys*, AFS/Akanaluminium, Stockholm, 1990.
28. P. Skjerpe: *Metall. Trans. A.*, 1987, vol. 18A, pp. 189-200.
29. H. Kosuge and I. Mizukami: *Journal of Japan Institute of Light Metals*, 1975, vol. 25, pp. 48-58.
30. L.F. Mondolfo: *Aluminium Alloys: Structure and Properties*, Butterworth and Co., London, 1976.
31. A.L. Dons: *Z. Metallkd.*, 1984, vol. 75, pp. 170-74.
32. H. Jones: *Mater. Sci. Eng.*, 1969, vol. 5, pp. 1-18.
33. P. Liu and G.L. Dunlop: *Mater. Sci. Technol.*, 1986, vol. 2, pp. 1009-18.
34. P. Liu and G.L. Dunlop: *Aluminum Alloys—Their Physical and Mechanical Properties*, Trans Tech. Publications Inc., Zurich, Switzerland, 1986, vol. 1, pp. 3-16.
35. L. Narayanan, F.H. Samuel, and J.E. Gruzleski: *Metall. Mater. Trans. A*, 1994, vol. 25A, pp. 1761-73.
36. R. Mackay and J.E. Gruzleski: *Int. J. Cast Met. Res.*, 1997, pp. 131-45.
37. S. Tang and T. Sritharan: *Mater. Sci. Technol.*, 1998, vol. 14, pp. 738-42.
38. H. Kosuge and I. Mizukami: *Journal of Japan Institute of Light Metals*, 1975, vol. 25, pp. 48-58.
39. W.B. Pearson: *Handbook of Lattice Spacings and Structure of Metals and Alloys*, Pergamon Press, London, 1967.
40. C.J. Simensen and R. Vellasamy: *Z. Metallkd*, 1977, vol. 68, pp. 426-31.
41. R. Ferro and A. Saccone: *Physical Metallurgy*, R. Cahn and P. Hansen, eds., North-Holland Pub., Amsterdam, 1996, [vol. 1], p. 206.
42. B. Yang, D. Stefanescu, and J. Leon-Torres: *Metall. Mater. Trans. A*, 2001, vol. 32A, pp. 3065-76.
43. ASM Specially Handbook: *Aluminum and Aluminum Alloys*, J. Davis, ed., ASM International Materials Park, OH, 1994.
44. H.D. Brody and M.C. Flemings: *Trans. TMS-AIME*, 1966, vol. 236, p. 615.
45. T.W. Clyne and W. Kurz: *Metall. Trans. A*, 1981, vol. 12A, pp. 965-71.
46. W. Kurz and D. Fisher: *Fundamentals of Solidification*, Trans Tech Publications, Aedermannsdorf, Switzerland, 1986, p. 129.
47. C. Potard, G. Bienvenu, and B. Schaub: *Proc. Sympos. on Thermodynamics of Nuclear Materials*, Vienna, 4-8 Sept. 1967, The International Atomic Energy Agency, Vienna, 1968, pp. 809-23.
48. I. Miki and H. Warlimont: *Z. Metallkd*, 1968, vol. 59, pp. 254-64.
49. D.J. Allen and J.D. Hunt: *Metall. Trans. A*, 1979, vol. 10A, pp. 1389-97.
50. M.J. Aziz: *J. Appl. Phys.*, 1982, vol. 53, pp. 1156-68.